

Supporting Information

DNA-origami line-actants control domain organisation and fission in synthetic membranes

Roger Rubio-Sánchez,^{*,†,‡,¶,§} Bortolo Matteo Mognetti,^{||} Pietro Cicuta,[§] and
Lorenzo Di Michele^{*,†,‡,¶,§}

[†]*Department of Chemical Engineering and Biotechnology, University of Cambridge,
Philippa Fawcett Drive, Cambridge CB3 0AS, United Kingdom*

[‡]*Department of Chemistry, Molecular Sciences Research Hub, Imperial College London,
London W12 0BZ, United Kingdom*

[¶]*fabriCELL, Molecular Sciences Research Hub, Imperial College London, London W12
0BZ, United Kingdom*

[§]*Biological and Soft Systems, Cavendish Laboratory, University of Cambridge, JJ Thomson
Avenue, Cambridge CB3 0HE, United Kingdom*

^{||}*Interdisciplinary Center for Nonlinear Phenomena and Complex Systems, Université libre
de Bruxelles (ULB), Campus Plaine, CP 231, Blvd. du Triomphe, B-1050 Brussels,
Belgium*

E-mail: rmr44@cam.ac.uk; ld389@cam.ac.uk

Methods

Electroformation of Phase-separating Giant Unilamellar Vesicles

Electroformed vesicles^{1,2} were prepared in a 300 mM sucrose solution in MilliQ water as reported previously.³ Briefly, lipid mixtures were composed of 1,2-dioleoyl-sn-glycero-3-phosphocholine (DOPC, chain melting temperature -17°C ; Avanti Polar Lipids), 1,2-dipalmitoyl-sn-glycero-3-phosphocholine (DPPC, chain melting temperature 41°C ; Avanti Polar Lipids), and cholesterol (Sigma-Aldrich) at 4:4:2 molar ratio. In addition, fluorescent Texas Red-DHPE (Invitrogen) was included in the lipid mixtures at 0.8% molar ratio, which preferentially enriches L_d domains. Subsequently, 45 μL of lipid mixtures ($4\text{ mg}\cdot\text{mL}^{-1}$) were spread on the conducting side of clean indium tin oxide (ITO) slides heated above 60°C . The slides were placed in a dry silica dessicator for ~ 1 hour and then assembled into an electroformation chamber using a ~ 1 mm thick polydimethylsiloxane (PDMS) spacer enclosing approximately 400 μL of degassed sucrose buffer. Electroformation chambers were placed in a pre-heated oven at $T > 60^{\circ}\text{C}$ and connected to a frequency generator using clamps. The electroformation program consisted of a sinusoidal alternating current (AC), voltage amplitude of 2V, and frequency of 10 Hz for 2 hrs followed by 2 Hz for 1 hr. Finally, vesicles were retrieved and stored at room temperature in the dark to prevent photo-bleaching and photo-oxidation.

Design of line-active DNA origami nano-devices

DNA anchoring modules were designed using the NUPACK suite software,⁴ and are based on previously reported nano-devices.^{3,5} For the line-active plates, we used a modified version of the Rothmund Rectangular Origami.⁶ Membrane attachment was achieved by functionalising the origami plates with the Picasso software,⁷ which allowed to precisely engineer the spatial location of membrane-anchoring points. To that end, the sequence of specific staples was extended on their 3' end to include docking domains that would project outwards on

a single face of the planar origami. These overhangs hybridised to sticky-end overhangs of dsDNA anchoring modules. On the opposite face of the origami, 5' end extensions were incorporated in eight DNA staples to include a domain capable of binding a fluorescent oligonucleotides for confocal imaging. In the case of line-partitioning measurements (Fig. 2 in the main text), 5'-end extensions were used to attach a strand with $3\times$ binding sites for fluorescent oligonucleotides, in order to increase the signal-to-noise upon confocal acquisition.

Assembly of DNA Nanostructures

Lyophilised DNA oligonucleotides (Integrated DNA Technologies [IDT], Eurogentec, and Biomers), were reconstituted to a nominal concentration of $100\ \mu\text{M}$ in Tris – Ethylenediaminetetraacetic acid (EDTA) buffer ($1\times$ TE: $10\ \text{mM}$ Tris + $1\ \text{mM}$ EDTA, pH 8.0).

DNA anchor-modules were subjected to a slow quenching temperature ramp on a TC-512 thermal cycler (95°C down to 4°C at a rate of $-0.5^\circ\text{C}\ \text{min}^{-1}$) in a buffer containing $1\times$ TE + $100\ \text{mM}$ NaCl.

Origami plates self-assembled with a temperature quenching ramp in a total volume of $100\ \mu\text{L}$ containing 7249-bp single-stranded circular viral template (M13mp18, tilibit nanosystems) as scaffold ($10\ \text{nM}$) as well as core and modified stapling oligonucleotides, in the presence of a folding buffer composed of $1\times$ TE + $12.5\ \text{mM}$ MgCl_2 . Staples capable of membrane-attachment were included at $100\times$ excess, while core staples as well as those part of the fluorescent beacon were present at a $10\times$ excess.

Thermal annealing was performed in a TC-512 thermal cycler. Samples were incubated at 80°C for 5 minutes to promote denaturing and suppress secondary structures. Subsequently, the temperature was decreased to 60°C , and later on to 40°C with a rate of $0.3125^\circ\text{C}\cdot\text{min}^{-1}$. Finally, the temperature was brought down to 20°C .

Purification of DNA origami

Self-assembled rectangular DNA origami plates underwent 3 cycles of PEG-induced precipitation⁸ to remove excess staples. To that end, DNA origami samples were brought to a volume of 250 μL with folding buffer ($1\times$ TE + 12.5 mM MgCl_2) and mixed 1:1 to a final volume of 500 μL with a solution containing 8000 Da polyethylene glycol (PEG8000, Sigma-Aldrich) at 15% (w/v) in $1\times$ TE + 505 mM NaCl. After mixing *via* tube inversion, the solution was centrifuged (16,000g) at room temperature for 25 minutes. The supernatant was discarded, the pellet was reconstituted in 250 μL folding buffer, and the solution incubated at room temperature for at least 30 minutes before proceeding with the next precipitation cycle. After 3 cycles, the origami pellet was reconstituted to a final concentration of 10 nM and stored at room temperature in the dark to prevent photobleaching.

Vesicle Functionalisation with DNA line-actants

Pre-assembled anchoring modules were incubated overnight with vesicles (16.7 μL of DNA solution + 9.2 μL GUV solution, both prepared as indicated in “Electroformation of Phase-separating Giant Unilamellar Vesicles” and “Assembly of DNA Nanostructures”, respectively, in 57.4 μL of buffer resulting in an iso-osmolar mixture. This functionalization procedure has been previously used in several works, and ensures optimal attachment of DNA constructs to GUVs^{3,9-13}. Following the functionalisation of GUVs with anchor modules, the purified DNA origami tiles were heated up to $\sim 40^\circ\text{C}$ for 10 minutes, followed by gentle vortexing to destabilise aggregates, and 8.35 μL were mixed with a second correction buffer (10 μL). The mixture was gently added to the GUVs decorated with anchoring modules, resulting in an iso-osmolar solution ($1\times$ TE + 99.2 mM NaCl + 0.8 mM MgCl_2 + 86.2 mM Glucose) that was left under rotation for at least 3 hours to allow for origami hybridisation to the anchor modules, and hence attachment of the tiles to the GUVs. In all cases, the membrane-bound anchor modules were in a nominal $\sim 1.5\times$ excess of the origami binding capacity, to ensure that all available overhangs on the origami are linked to the correspond-

ing anchoring modules. Finally, the GUVs were placed in silicone wells for imaging, and allowed to sink for at least ~ 15 minutes before imaging.

Agarose Gel Electrophoresis (AGE)

Agarose gels were prepared at 2% (weight) in Tris-Borate-EDTA (TBE, Sigma-Aldrich, 89 mM Tris-borate, 2 mM EDTA, pH 8.3) buffer. The mixture was dissolved *via* heating. Subsequently, SYBR Safe DNA gel stain (Invitrogen) was added at 0.1% (volume) mixed through gentle swirling, and was later casted to a thickness of approximately 5 mm. After setting for 1 hour, the gel was placed in an electrophoresis chamber and covered with TBE. 20 μ L of annealed origami (Supplementary Fig. 1) or anchor-module samples (Supplementary Fig. 13) were loaded onto the gel alongside a DNA reference ladder (100 bp GeneRuler, Thermo Scientific). Control samples included origami staples and annealed scaffold. The electrophoresis chamber was placed on ice, and a potential of 75 V (3.75 V cm^{-1}) was applied for 90 minutes. Finally, the gel was imaged with a GelDoc-It system containing a UV lamp for illumination.

Fluorescence Microscopy of GUVs

Clean glass slides (15 min sonication cycles Hellmanax III 2%/isopropanol/MilliQ water) were passivated by covering with a solution containing bovine serum albumin (BSA) at 0.1% (w/v) and incubating in a pre-heated oven ($T > 60^\circ\text{C}$) for an hour. Excess of BSA was removed with thorough rinsing with milli Q water. Silicone incubation chambers (Sigma-Aldrich) were stuck to passivated slides and sealed with DNase-free tape to prevent evaporation.

Confocal imaging was performed at 1400 Hz, averaging over 10 frames, with a Leica TCS SP5 confocal microscope and an HC PL APO CORR CS $40\times / 0.85$ dry objective from

Leica. Alexa488 (excitation maximum - 495 nm; emission maximum - 520 nm) signal was acquired exciting with an Ar-ion laser (488 nm).

Epifluorescence microscopy was carried out at 10 frames per second using a home-built Nikon Eclipse Ti-E inverted microscope equipped with a 40 \times objective lens from Nikon (Plan APO λ , NA 0.95) and a Grasshopper3 GS3-U3-23S6M camera from Point Gray Research. Illumination in this set-up was provided by single-colour light emitting diodes (LEDs) through a filter set for Texas Red.

Atomic Force Microscopy

Atomic Force Microscopy (AFM) was used to confirm the correct assembly of DNA origami plates. After the temperature ramp, 10 μ L of DNA origami samples at \sim 1 nM (1 \times TE + 12.5 mM MgCl₂) were casted on top of a freshly cleaved mica sheet, which was previously fixed onto a microscope slide and cleaved with sticky-tape. The sample was incubated for 10 minutes before two cycles of washing. These consisted of adding 300 μ L of ultrapure water on top of the mica sheet, followed by drying under a gentle nitrogen flow for 3 minutes. Micrographs were acquired using a MFP-3D Infinity AFM (Asylum Research) in Dry Tapping Mode. AFM silicon probes (BudgetSensors) bearing an aluminum reflex coating had a nominal frequency of \sim 300 kHz and a stiffness of 40 N \cdot m⁻¹. Data processing was performed with Gwyddion¹⁴ by levelling the data and applying mean plane subtraction and row alignment.

Supplementary Note I: Membrane biophysics considerations for line-actant engineering

It is key to our line-actant design to compare the size of the DNA nanostructures with the finite thickness of the interface between two phases, and to ensure that same-type anchor-points are close together and separated from those with opposite partitioning tendency by a distance that exceeds the interface width. To that end, we estimated the thickness of the interface using the correlation length (ξ), derived as¹⁵

$$\xi \approx A \left| \frac{T - T_c}{T_c} \right|^{-\nu} \quad (\text{S1})$$

where ν is a critical exponent, A is an amplitude factor, T is the temperature, and T_c is the critical temperature, defined as that where membranes with a suitable composition Φ_c exhibit fluctuations with length scales that diverge and the line tension vanishes. The critical exponent has been shown, within experimental error, to be consistent with the 2-D Ising model prediction of $\nu = 1$,¹⁵ while the amplitude factor (A) is given by $A = f^{(-)} \cdot \xi_0$ for $T < T_c$, with $f^{(-)} \approx 0.17$ as a dimensionless factor, and $\xi_0 \approx 1$ nm (approximately the diameter of a lipid head group).¹⁶

In our implementation, for phase-separating membranes with a miscibility transition temperature (T_m) close to the critical temperature, $T_m \sim T_c$ can be assumed. Indeed, we worked with vesicles prepared at 4:4:2 (DOPC/DPPC/Chol), whose T_m ($\sim 33 \pm 1^\circ\text{C}$) has been shown to change only slightly with composition,² thus suggesting proximity to the critical point (Φ_c, T_c). It is therefore possible to obtain a sufficiently good approximation of ξ at room temperature ($T \sim 25^\circ\text{C}$) with Eq. S1 using $T_m \approx T_c$, leading to an estimated width of the interface of ~ 8 nm.

Supplementary Note II: Data acquisition and Data analysis

Data Acquisition

DNA-functionalised GUVs were placed in silicone incubation chambers and allowed to sediment on the bottom for at least 10 minutes prior to imaging. The chambers were sealed with sticky-tape to prevent evaporation.

Confocal Microscopy

Confocal micrographs were processed to assess the line-accumulation tendencies of our DNA nano-devices. To that end, we acquired z-stacks of fields of view $64.84 \mu m \times 64.84 \mu m$ with slice thicknesses of $0.5 \mu m$. The size of the field of view is the largest our instrument can image at the fastest scanning rate of 1400 Hz. Screening and selection of imaged vesicles was underpinned by two criteria:

1. Vesicles were smaller than the size of the field of view and bigger enough such that Brownian motion was negligible within the acquisition timescales of a few minutes per GUV.
2. The orientation of the vesicle was such that a sharp interface separating the L_d and L_o domains was visible at the equatorial cross-section of the GUV, thus enabling quantitative processing.

In view of the size cut-off introduced by the first criterion, resulting in an experimental relevant range of radii of $5 < R < 25 \mu m$, our model has accounted for the influence of GUV radius on the physics of line-accumulation.

Epifluorescence Microscopy

Epifluorescence micrographs were acquired to measure the ability of DNA line-actants to stabilise domains against coalescence. Passivated slides with GUV-containing imaging chambers were placed on top of a copper plate connected to a Peltier element and fixed with aluminum tape. The chambers were then heated to $T = 37^\circ\text{C}$, allowed to equilibrate for ~ 5 minutes, and cooled down to $T = 25^\circ\text{C}$. The chambers were subsequently placed on the microscope stage, and the vesicles were allowed to equilibrate for ~ 3 hours. Acquisition was done using a custom-built script that enabled the automated manipulation of the instrument in terms of time and illumination at previously hand-picked positions.

Data Analysis

Quantitation of line-accumulation tendencies across variants of line-active DNA nano-devices

Equatorial micrographs of GUVs were manually selected from confocal z-stacks prior to analysis. Image processing is underpinned by a MATLAB segmentation pipeline that allows to identify membrane radial intensities and extract data points around the boundaries between lipid domains.

The custom-built user-assisted software loads equatorial micrographs and uses a Gaussian blurring routine for noise removal and to facilitate segmentation. Aided by a Graphical User Interface, three positions along the membrane circumference are manually chosen: i and ii) are rough locations of the two interfaces and iii) is a position along the L_d domain. Estimated values are subsequently used to enclose the membrane within a ring, allowing the software to extract radial profiles along the membrane contour in steps of $\pi/900$. For each profile, the position of the membrane is estimated using a Gaussian fit. Estimated positions are then processed with a circle-fitting routine. Specifically, a subset of points extracted from radial profiles (those within $\pm 5\%$ of the estimated average radius of the vesicle) are fitted to

a circle, which we used as a final estimate for the membrane positions. These enabled us to extract from the unprocessed raw images the average fluorescence intensity of the membrane *via* numerical integration around the position of the bilayer (± 2 pixels).

We subsequently extracted segments from the radial fluorescence intensity profile corresponding to the line-interfaces *via* the user-provided rough locations of the two boundaries. The traces were extracted around a defined width of $\pm 5 \mu m$ from the estimated location of the interface, which we then fitted to an empirical model to better approximate the location of the line-interface. To that end, we model the fluorescence profile of the L_d - L_o interface as the sum of a step function with a rectangular function, both centred at the location of the boundary. Owing to diffraction-limited blurring, the sum of these functions is convolved with a Gaussian.

We thus fit our fluorescence intensity data to the sum of a Gaussian and a sigmoidal function as

$$I(x) = A \exp \left[- \left(\frac{x - B}{C} \right)^2 \right] - D \tanh \left[\frac{x - B}{C} \right] + D + E \quad (\text{S2})$$

where A and D are the amplitude of the Gaussian and sigmoidal, respectively, and C is the width. From the fit, we estimate the location at which the interface is centred, namely B . Finally, vector re-sampling is applied to construct an interfacial intensity trace around the location of the interface ($x = 0$) around a width of $\pm 4 \mu m$ at every $0.05 \mu m$. Line-interface traces were then averaged and fitted to Eq. S2, as collated in Fig. 2 (main text) and Supplementary Fig. S8.

From the fitted parameters A, C, D , and E , we compute the line partitioning coefficient $K_{p,int}$. First, the bulk L_d fluorescence intensities were estimated as $I_{L_d} = D + E$ and $I_{L_o} = E$. Then, the average fluorescence intensity of the line-interface (I_{int}) was approximated with

$$I_{\text{int}} = \frac{(A + E)C\sqrt{\pi}}{\delta} \quad (\text{S3})$$

In other words, we calculated the area under the Gaussian (i.e. the fluorescence intensity across the whole finite thickness of boundary) and divided it by the nominal length along which the origami can accumulate (i.e. $\delta = \xi + \ell$, where ℓ is the spacing between dC and sT anchoring regions in the origami).

We then define a mean number density $\rho = N/A_{\text{GUV}}$ as the total number of origami in a vesicle with surface area A_{GUV} . Similarly, it is possible to define mean number densities at the line-interface ($\rho_{\text{int}} = N_{\text{int}}/A_{\text{int}}$) and in $L_{\text{o(d)}}$ phases ($\rho_{L_{\text{o(d)}}} = N_{L_{\text{o(d)}}}/A_{L_{\text{o(d)}}}$).

Thus, line-interface partition coefficients can be obtained as

$$K_{\text{p,int}} = \frac{\rho_{\text{int}}}{\rho} \quad (\text{S4})$$

Assuming that the measured fluorescence intensities are proportional to the membrane densities, such that $\rho_{\text{int}} = \alpha I_{\text{int}}$ and $\rho_{L_{\text{o(d)}}} = \alpha I_{L_{\text{o(d)}}$, we can write

$$\rho = \alpha \frac{I_{\text{int}}A_{\text{int}} + I_{L_{\text{o}} }A_{L_{\text{o}}} + I_{L_{\text{d}}}A_{L_{\text{d}}}}{A_{\text{GUV}}} \quad (\text{S5})$$

which applied to Eq. S4 leads to

$$K_{\text{p,int}} = \frac{I_{\text{int}}A_{\text{GUV}}}{I_{\text{int}}A_{\text{int}} + I_{L_{\text{o}}}A_{L_{\text{o}}} + I_{L_{\text{d}}}A_{L_{\text{d}}}} \quad (\text{S6})$$

We used Eq. S6 to compute the experimental line-partitioning coefficients, collated in Supplementary Fig. S5. To that end, we assumed the vesicles (with radius R) were perfectly Janus with two hemispherical domains, thus having $A_{\text{GUV}} = 4\pi R^2$, $A_{L_o} = A_{L_d} = 2\pi R^2$. In turn, we estimate the area of the interface using $A_{\text{int}} = 2\pi R\delta$, i.e. the length of the line-interface ($L = 2\pi R$) multiplied by $\delta = \xi + \ell$ (the width available for tile displacements in the direction orthogonal to the line-interface). Recalling that from the fit with Eq. S2 we estimate $I_{\text{int}} = \frac{(A+E)C\sqrt{\pi}}{\delta}$, $I_{L_d} = D + E$, and $I_{L_o} = E$, Eq. S6 becomes:

$$K_{\text{p,int}} = \frac{2R\frac{(A+E)C\sqrt{\pi}}{\delta}}{(A+E)C\sqrt{\pi} + R(D+2E)}. \quad (\text{S7})$$

To compute the values of $K_{\text{p,int}}$ shown in Fig. 2c, we chose $\xi = 8$ nm (see Supplementary Eq. S1) and $\ell = 30$ nm, for $6\times$ and $12\times$ tiles, or $\ell = 25$ nm for $24\times$ tiles. While the latter value is defined by the origami design, substantial uncertainty may affect the estimate of the interface thickness ξ . To determine how this uncertainty propagates to the estimation of $K_{\text{p,int}}$, in Supplementary Fig. 8 we show the results obtained using the lower and upper physical bounds of ξ , with the lower bound being $\xi = 0$ ($\delta = \ell$, negligible interface thickness) and the upper bound being $\xi = \ell$ ($\delta = 2\ell$, determined by noting that $\xi > \ell$ would prevent line accumulation). $K_{\text{p,int}}$ values are, for all choices of ξ , within a factor two of each other and preserve the same trends with respect to tile design.

Quantification of lipid domains stabilisation

To assess the line-action of DNA nanostructures, DNA-decorated vesicles were imaged after temperature quenching using epifluorescence microscopy. Micrographs of several fields of view were acquired for each sample, and individual micrographs were analysed using a custom-built MATLAB script for quantitative assessment.

The script, which operates in a user-assisted fashion, loads a frame selected at random from a set containing images for all conditions (Fig. 3b in the main text), thus blinding the data and minimising human bias. The Graphical User Interface then asks the user to input values for:

- The number of vesicles that are de-mixed (N_{DM}).
- The number of vesicles that are homogenously mixed (N_M).
- The number of vesicles with Janus morphology (i.e. with only two macroscopic domains) (N_J).
- The number of vesicles with two-dimensional Pickering emulsions (i.e. with more than two macroscopic domains) (N_{PE}).

Once all frames have been allocated values for each of these conditions, the script computes the fraction of vesicles featuring more than two stable domains (F) with

$$F = \frac{N_{PE}}{N_{PE} + N_J + N_M}, \tag{S8}$$

Supplementary Note III: Theoretical estimation of line-partitioning

Throughout this section, we derive a numerical model to predict line-partitioning of our DNA-origami line-actants. Thus, by comparing predictions from theory using experimental parameters (see Table S6) with the experimental observations (Figure 2 of the main text), we infer the surface coverage of tiles on GUVs (σ), which we subsequently use to compute the fraction of tiles at the line-interface (ϕ).

We consider N_{int} tiles covering a line-interface of length L . The partition function of the system, Z_{int} , accounts for the free-energy contribution given anchor–bilayer interactions ($\Delta G_{\text{p,int}}$) as well as a term ($z_{\text{int,conf}}$) accounting for the configurational space available to each tile. Thus,

$$Z_{\text{int}} = \frac{[q_1 \exp(-\beta \Delta G_{\text{p,int}}) z_{\text{int,conf}}]^{N_{\text{int}}}}{N_{\text{int}}!} . \quad (\text{S9})$$

Equation S9 assumes that lipid–lipid interactions are not altered by the presence of anchors. In addition, q_1 lumps all single–tile contributions with the exclusion of anchor–bilayer interactions. We write the configurational free–energy *per* tile as follows

$$z_{\text{int,conf}} = \Delta\theta [\delta(L - N_{\text{int}}L_1)] , \quad (\text{S10})$$

In the previous expression, $\Delta\theta$ refers to the angle describing the range of possible tile orientations with respect to the line-interface, δ is the distance range available for possible tile displacements orthogonal to the line, and L_1 is the width (short side) of the tile. δ is estimated using the distance between the two sets of anchor-points (ℓ) augmented by the finite width of the line-interface (ξ , see Fig. 1 in the main text and Supplementary Note I). We estimated $\Delta\theta$ by placing the centre of the tile on top of a straight line separating the two lipid phases, allowing us to consider all possible tile orientations with which all anchor-points are hosted on their favorable phase. Note that it is possible for a tile at the line-interface to expose some anchors to their unfavourable phase by paying an accessible free–energy cost (increasing the value of $\Delta G_{\text{p,int}}$). Therefore, in order to estimate an order of magnitude of systematic errors associated with the model, below we also consider tiles which can fully rotate while being at the line (i.e., $\Delta\theta = 2\pi$). Note also that in Eq. S10 we factorize the translational (parallel and orthogonal to the line-interface) and rotational

contributions while, in reality, rotational and translational degrees of freedoms are coupled (for instance, $\Delta\theta$ tends towards zero when two tiles enter into contact).

We then assess the equilibrium conditions between tiles in the bulk phases (modeled using two hemispheres with surface area $2\pi R^2$) and tiles at the line. We consider the dilute case in which, in the bulk phases, tile–tile interactions are negligible (note that Eq. S10 accounts for excluded volume interactions between tiles at the line-interface). Importantly, we do not consider the possibility for the tiles to increase the length L of the line, which we fix to $L = 2\pi R$. We argue that this is a reasonable assumption at low T , as supported by the simulations in Fig. 4 (main text). The chemical potentials in the three different locations (L_d , L_o , and L_d-L_o interface) are the same and equal to

$$\begin{aligned}
\beta\mu &= \log \frac{N_{\text{int}}}{(L - N_{\text{int}}L_1)\delta q_1 \Delta\theta} + \frac{N_{\text{int}}L_1}{L - N_{\text{int}}L_1} + \beta\Delta G_{\text{p,int}} \\
&= \log \frac{N_{L_o}}{(2\pi R)^2 q_1} + \beta\Delta G_{\text{p},L_o} \\
&= \log \frac{N_{L_d}}{(2\pi R)^2 q_1} + \beta\Delta G_{\text{p},L_d}
\end{aligned} \tag{S11}$$

where $N_{L_o(L_d)}$ and $\Delta G_{\text{p},L_o(L_d)}$ are, respectively, the number of tiles and the anchors-bilayer free energy contributions *per* tile in the $L_o(L_d)$ phase. Equations S11 allow calculating N_{int} . The problem can be simplified by assuming that the tiles at the boundary lines do not deplete the number of tiles in the bulk phases, $N_{\text{int}} \ll N_{L_o}, N_{L_d}$, and therefore do not change the chemical potential of the bulk phases as compared to the $N_{\text{int}} = 0$ case. Under these assumptions, using $N = N_{L_o} + N_{L_d}$ in the second equality of Equations S11 with $\rho = N/(4\pi R^2)$, we simplify the chemical potential as follows

$$\beta\mu = \log \frac{\rho/(q_1\pi)}{\exp(-\beta\Delta G_{\text{p},L_o}) + \exp(-\beta\Delta G_{\text{p},L_d})} \tag{S12}$$

The fraction of line-interface covered by tiles, assuming that tiles remain orthogonal to the line-interface, is

$$\phi = N_{\text{int}} \frac{L_1}{L} \quad (\text{S13})$$

which we then obtained using Eq. S12 in the first of the equalities in S11, which leads to

$$\frac{\phi}{1-\phi} \exp\left[\frac{\phi}{1-\phi}\right] = \frac{2L_1\delta\Delta\theta}{2\pi} \frac{\exp(-\beta\Delta G_{\text{p,int}})}{\exp(-\beta\Delta G_{\text{p},L_o}) + \exp(-\beta\Delta G_{\text{p},L_d})} \rho \equiv \Lambda\rho \quad (\text{S14})$$

from which ϕ can be calculated numerically. Note that, in a Langmuir-like approach that would not consider the second term in RHS of first equality in S11, the previous equation would result in

$$\phi = \frac{\Lambda\rho}{1 + \Lambda\rho}. \quad (\text{S15})$$

Given ϕ , the theoretical prediction of the line-partitioning coefficient is calculated with

$$K = \frac{\rho_{\text{int}}}{\rho} = \frac{\phi}{\rho L_1 \delta}. \quad (\text{S16})$$

We now estimate the anchors-bilayer free-energy contributions $\Delta G_{\text{p},L_o}$, $\Delta G_{\text{p},L_d}$, and $\Delta G_{\text{p},L_o}$. The experimental $K_{\text{p,int}}$ can be readily compared to the increase in surface density required to saturate line-interfaces. As done previously in our work on regulating the partitioning of DNA nano-devices in lipid domains,³ we define a free-energy of partitioning as the shift associated with moving a single DNA tile from L_d to either the L_d - L_o interface ($\Delta G_{\text{p,int}}$) or L_o ($\Delta G_{\text{p},L_o}$). In particular, this choice sets $\Delta G_{\text{p},L_d}$ to $\Delta G_{\text{p},L_d} = 0$. To achieve

line-accumulation, dC anchor-points need to be translocated to L_o while maintaining sT modules in L_d so to induce the correct orientation of the line-actants. Thus, we calculate the free energy of line partitioning with $\Delta G_{p,\text{int}} = \sum_i \Delta G_{p,L_o}^{\text{idC},i}$, where the index i runs over all the dC anchors in the origami. In the case of enriching L_o domains, the free energy of partitioning is additive in the contributions of all (j) hydrophobic anchors featured in the nanostructure given by $\Delta G_{p,L_o} = \sum_j \Delta G_{p,L_o}^j$. Thanks to the work of Jungmann and co-workers,¹⁷ one can also account for the efficiency of staple addressability in the origami by weighting the free-energy contribution of a given anchor-point (see Table S7) with the probability (p) of incorporation as

$$\Delta \tilde{G}_{p,\text{int}} = \sum_i p_i \Delta G_{p,L_o}^{\text{idC},i} \quad (\text{S17})$$

To account for possible systematic errors (as done for the rotational configuration contributions to the free-energy), also in view of the fact that we expect the line-interface to be enriched by tiles featuring more anchors, if not all, than the averaged values, in the following we consider both ΔG and $\Delta \tilde{G}$. All parameters employed in the theoretical model are summarised in Table S6. Note that the average incorporation probabilities for dC and sT anchoring staples are similar across the three tile designs adopted (see Table S8), implying that incomplete staple incorporation is unlikely to produce a substantial unbalance in the number of available binding sites available for the two types of anchoring modules.

Figure S5 (a,c, and e) report the theoretical predictions of the line-partitioning coefficient ($K_{p,\text{int}}$) as a function of the surface coverage ($\sigma = \rho L_1 L_2$). By intersecting these plots with the experimental values $K_{p,\text{int}}^{n \times}$ (including an uncertainty on the latter quantified with the standard deviation, $\delta K_{p,\text{int}}$, see Table S6), we predict the following surface coverages, also summarised in Fig. S6: $\sigma_{\text{theory}}^{6 \times} < 0.032$, $0.015 < \sigma_{\text{theory}}^{12 \times} < 0.093$, and $0.029 < \sigma_{\text{theory}}^{24 \times} < 0.144$. These values are consistent with the approximated coverage ($\sigma_{\text{exp}} \sim 0.05$) using the

stoichiometric parameters employed in our experimental implementation (see Methods in the main text). The increase of the predicted σ in the 12 \times and 24 \times designs can be explained by a higher affinity of the tiles for the lipid membranes. This observation is consistent with the absolute values of the fluorescent signals reported in Fig. S8.

Using the inferred values of ρ , $\rho = \sigma/(L_1L_2)$, we can then calculate the fraction of occupied line-interface (ϕ) using Eq. S14 (see Fig. S5, panels b,d, and f). In particular, we find: $\phi^{6\times} < 0.537$, $0.508 < \phi^{12\times} < 0.84$, and $0.88 < \phi^{24\times} < 0.935$. These results show how the experimental values of $K_{p,int}$ are indicative of the regulatory influence of anchor number in line-partitioning, demonstrating an increase in line-accumulation as a function of the number of anchors. Finally, our observations also prove that line-partitioning is mainly driven by the anchor-bilayer affinity, supporting the biophysical model proposed in this contribution.

Šulc and co-workers have recently demonstrated that 2D origami tiles spontaneously bend in the direction orthogonal to that of the double helices, as a result of steric repulsion between overhangs present only on one face.¹⁸ Bending of our membrane-confined tiles would result in a lower effective width L_1 , and thus impact the estimation of $z_{int,conf}$.

Because of the even distribution of anchoring points on their surface, 24 \times and 12 \times tiles would need to break connections with the membrane in order to bend, or force a curvature on the lipid bilayer itself. These occurrences are however energetically prohibitive, given that the typical free energies associated with tile bending ($\sim 5k_B T$ ¹⁸) are small compared with the free-energies penalties associated to i) de-hybridising the tile overhangs from the anchor modules tethered to the lipid bilayer ($\sim 40k_B T$ per overhang, as computed with NUPACK⁴), ii) pulling out one of the hydrophobic anchors from the bilayer (~ 20 to $30k_B T$ per anchor^{19,20}), and iii) bending the membrane ($\sim 20k_B T$ for liquid-disordered lipid membranes²¹). Due to the anchoring points being localised close to the long axis of the tile, 6 \times designs could potentially retain a bent configuration while anchored to the membrane. It should be however noted that Šulc and co-workers observed spontaneous curvature on

origami featuring a full array of 169 overhangs. We would thus speculate that the effect is likely negligible for the $6\times$ design, which only has 12 overhangs.

We thus conclude that none of the tested tile designs are likely to acquire curved configurations while on the membranes, justifying the interpretation of L_1 as the nominal tile width.

Supplementary Note IV: Implementation of Ising-type coarse-grained Monte Carlo simulations

The model

Lipid bilayer. Phase separation in lipid bilayers has been traditionally studied using the Ising model.²²⁻²⁵ In particular, the thermodynamic quantities of the system and the line morphology close to the critical point are described by the Ising universality class.¹⁵ A bilayer is modeled with a 2-dimensional lattice in which each site carries a fluctuating spin (s_i , $s_i = \pm 1$), representing the phase found in a unit cell (L_o or L_d). Neighboring spins (s_i and s_j) contribute to the energy of the system through a $-Js_i s_j$ term, where J is an energetic parameter favouring the alignment of the spins and, therefore, hampering the formation of boundaries between different phases. The total configurational energy then reads as

$$H_{ss} = -\frac{J}{2} \sum_i \sum_{j \in \nu(i)} s_i s_j \quad , \quad (\text{S18})$$

where $\nu(i)$ is the list of neighboring sites of i . We use a triangular lattice, in which each site interacts with six neighbors, and employ periodic boundary conditions. The non-dimensional parameter controlling the phase behavior of the system is given by $x = J/(k_B T)$. In particular, phase separation is induced when decreasing the temperature below a critical value (T_c) corresponding to $x_c = \frac{\log 3}{4}$ ($T_c = \frac{J}{k_B x_c}$). The spin update implemented by the simulation

algorithm (see below) conserves the total magnetization of the system defined as $M = \sum_i s_i$. The dynamics preserving M are consistent with the conservation of the number of lipid molecules of a given type.

Line-actants. We now describe the tiles' model and their implementation to the Ising model introduced above (see Fig. 4a of the main text). N_T is the number of tiles in the system. A tile covering a fraction of the bilayer is modeled by flagging a certain number of lattice sites as being covered by the specific tile. Accordingly, the position and orientation of the tiles are discretised variables. Following the design shown in Fig. 1b of the main text, each tile is approximated by 17 rows made of 15 lattice sites. As stated above, the rows are constrained to lay along one of the 6 directions of the lattice. A certain number of lattice sites covered by a tile will also host an anchor (shown in blue and red hexagons in Fig. 4a of the main text). The position of the anchors is fixed in the tile's reference frame. In particular, if the position of a tile is updated, the anchors will move accordingly.

We define by $i_{k,\alpha}^{(\text{sT})}$ and $i_{k,\alpha}^{(\text{dC})}$ ($k = 1, \dots, N_A$, $N_A = 6, 12$, or 24) the lattice hosting the k -th anchor of tile α of type sT and dC, respectively. The interaction of a spin with neighboring spins (Eq. S18) is not altered by the presence of a tile (in particular a lattice site can be occupied both by a spin and an anchor). An anchor hosted by site i interacts with s_i and all the spins found on a neighbor of i . In particular, an anchor of type sT and dC will contribute to the configurational energy with $-J_{\text{sT}}\tilde{s}(i_{k,\alpha}^{(\text{sT})})$ and $-J_{\text{dC}}\tilde{s}(i_{k,\alpha}^{(\text{dC})})$, respectively, where we defined $\tilde{s}(i) = s_i + \sum_{j \in \nu(i)} s_j$. By taking $J_{\text{sT}} > 0$ ($J_{\text{dC}} < 0$) we design sT (dC) anchors that interact favorably with the $s = 1$ ($s = -1$) phase. Finally, the total contribution of the tiles to the configurational free energy reads as follows

$$H_t = - \sum_{\alpha=1}^{N_T} \sum_{k=1}^{N_A} \left(J_{\text{sT}}\tilde{s}(i_{k,\alpha}^{(\text{sT})}) + J_{\text{dC}}\tilde{s}(i_{k,\alpha}^{(\text{dC})}) \right) + \sum_{\alpha < \beta} V_{\alpha,\beta}^{(\text{excl})} \quad (\text{S19})$$

where $V_{\alpha,\beta}^{(\text{excl})}$ is an excluded-volume interaction preventing a lattice site to be occupied by

more than one tile. Finally, the total configurational energy (H) of the model is given by

$$H = H_{ss} + H_t \quad . \quad (\text{S20})$$

Estimation of the model's parameters

The line tension of spin systems on the triangular lattice is calculated as in Ref.²⁶ based on the method of Zandvliet to calculate boundary free-energies.²⁷ The free-energy cost *per* spin along one of the principal directions, τ^* , reads as follows (see Eq. 9 in Ref.²⁶ with $A = 1$ and $B = X = Y = \exp(-2x)$)

$$\beta\tau^* = 4x + \log \frac{1 - e^{-4x}}{2} \quad (\text{S21})$$

Note that $\tau^* = 0$ if $x = x_c$. The previous equation is similar to an exact result calculated by Onsager (see Eq. 122a in Ref.²⁸) for the square lattice. By inverting the previous equation we obtain

$$x = \frac{1}{4} \log (1 + 2e^{\beta\tau^*}) \quad (\text{S22})$$

We estimate τ^* as $\tau^* = \tau \cdot \delta$, where τ is an experimental estimation of the line tension ($\tau \approx 1 \cdot \text{pN}^{15}$) and δ ($\delta = 5.77 \text{ nm}$) corresponds to the lattice spacing of the tile's geometry (see Fig. 1b, main text). Using these values in Eq. S22 provides $J = x k_B T \approx 0.55 k_B T$.

The non-dimensional parameters controlling the interactions between the tiles and the lipid bilayer are $x_a = \frac{J_a}{k_B T}$ and $x_b = \frac{J_b}{k_B T}$. These parameters are calculated from the experimental values of ΔG_{L_o} . In particular, given that each anchor interacts with 7 spins, we have

$$14x = \beta |\Delta G_{L_o}| \quad (\text{S23})$$

from which, using the experimental values of ΔG_{L_o} , we derive

$$J_{sT} = 0.136 k_B T \quad J_{dC} = -0.057 k_B T. \quad (\text{S24})$$

The previous equations neglect spin fluctuations (i.e. the fact that not all contacts could be favorable) and is strictly valid only in the limit in which temperatures tend to zero.

The simulation strategy

Each simulation cycle includes N_a attempts to implement one of the following MC moves ($N_a = N_l + 2N_T$, where N_l is the number of lattice sites and N_T the number of tiles):

1–Spin update (executed with probability $p = 0.9$). Spins are updated using Kawasaki dynamics.²⁹ This move proposes to exchange a pair of neighboring spins and accepts the new configuration according to a Metropolis test²⁹ with the change in configurational energy calculated using H_{ss} .

2–Tiles update (performed with probability $p = 0.1$). With equal probability, we either try to move a randomly selected tile along one of the six lattice orientations by δ , or we reorient the tile by $\pm 60^\circ$. The proposed configuration is accepted according to a Metropolis test with the change in configurational energy calculated using H_t .

Supplementary Figures

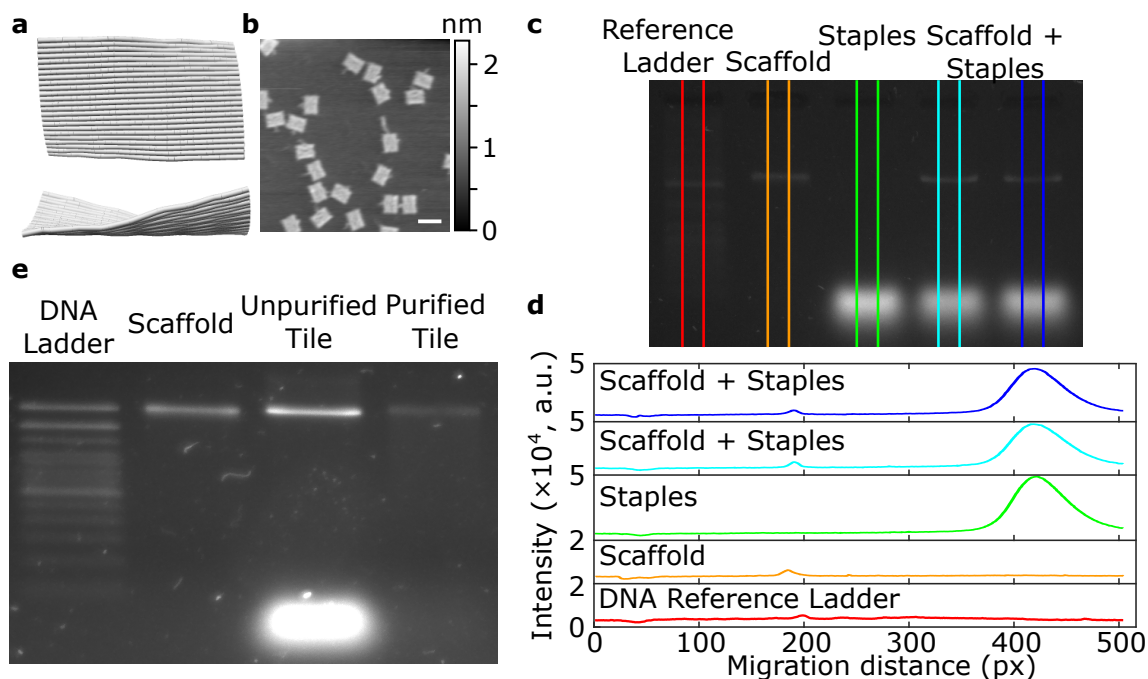


Figure S1: The origami methodology allows to assemble DNA-based tiles with programmable functionality. **a** Schematic representation of the top and side views of the Rothemund Rectangular Origami (RRO), as computed by Cando.^{30,31} **b** Atomic force micrograph confirming the assembly of nanostructures with rectangular conformations. Scale bar = 100 nm. **c** Micrograph of agarose gel electrophoresis of scaffold, staples, and origami assembled from mixtures of scaffold and staples annealed with the temperature quenching protocol described in the Methods. **d** Intensity profiles of image in panel (b) showing the migration pattern of the scaffold, staples, and the folded origami. **e** Micrograph of agarose gel electrophoresis of scaffold alongside unpurified and purified DNA tiles following three cycles of PEG-induced precipitation as described in the Methods, showing the successful removal of excess staples.

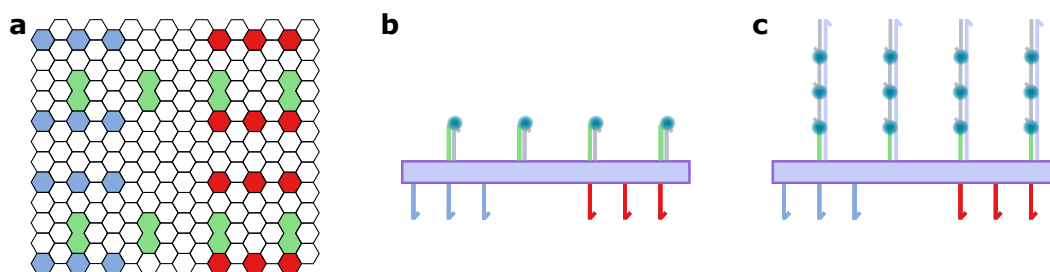


Figure S2: Location of fluorescent beacons in DNA line-actants. **a** Alexa488-conjugated oligonucleotides are incorporated to the RRO at 8 defined locations, highlighted in green in the hexagonal grid, by extending staples on their 5'-end to add docking domains, thus placing the fluorescent beacons on the face opposite to that hosting the anchor binding sites. **b** In the first design (used to collect z-stacks in Fig. 1 and Fig. 3 in the main text, we directly bind the fluorescent oligonucleotides (grey) to the docking domain (green), resulting in plates with ~ 8 fluorophores. **c** Our second design, used in measurements for line-partitioning quantitation (Fig. 2), the docking domain (green) in turn binds an extender strand which bears $3\times$ binding sites for the fluorescent oligonucleotide. In this case, each plate can feature up to $24\times$ fluorophores.

Line-actant design

3D Reconstruction for visualisation

Equatorial micrograph

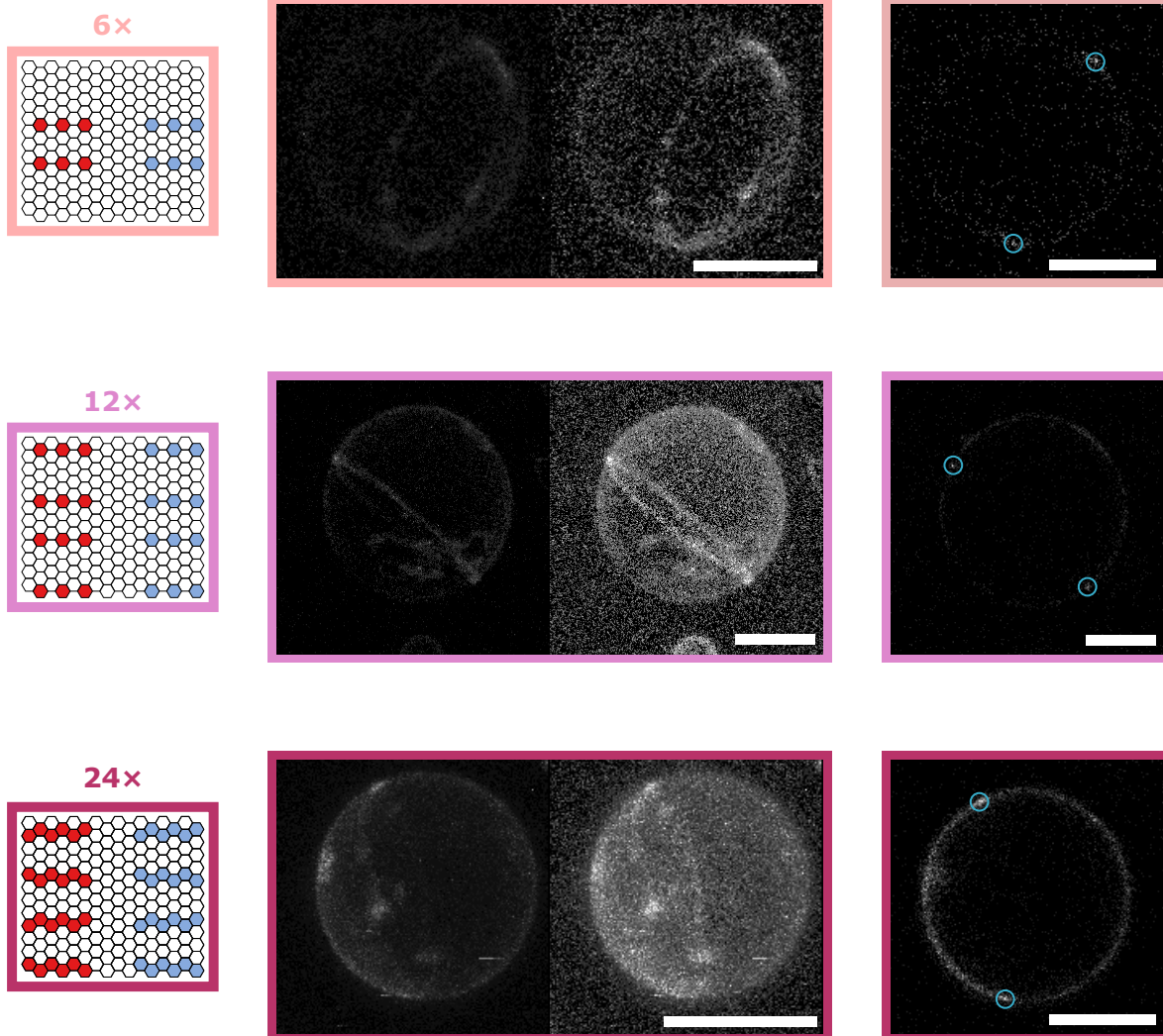


Figure S3: DNA plates with rationally-positioned binding sites for multiple sT and dC anchor modules enrich the line-interface of de-mixed GUVs. (Left) Schematic depictions of the tiles with the position of overhangs targeting sT (red) and dC (blue) anchoring modules. (Middle) 3D views of phase-separated vesicles with a Janus-like morphology showing line-accumulation of fluorescent (Alexa488) DNA plates with sets of either 6 \times , 12 \times , or 24 \times anchor-points, as reconstructed from confocal z-stacks using Volume Viewer (FIJI³²) with (right) and without (left) contrast enhancement. (Right) Representative equatorial confocal micrographs of GUVs with line-actant plates, highlighting with blue circles the location of the line-interfaces, which were used for quantitation of line-accumulation (see Fig. 2 in the main text). Scale bars = 10 μm .

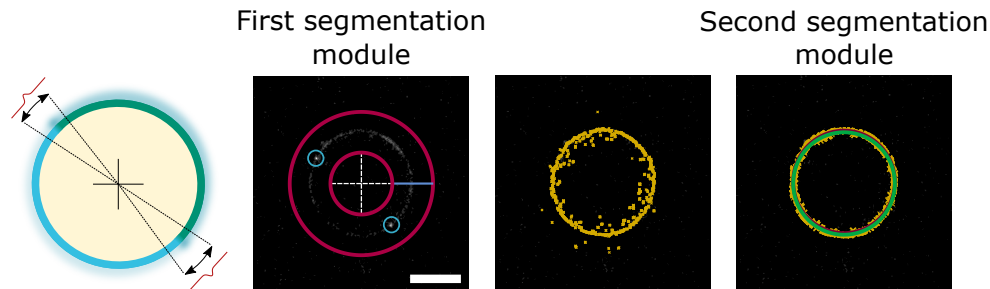


Figure S4: Micrograph segmentation allows to reconstruct the interfacial fluorescence intensity profile. The analysis pipeline operates on equatorial micrographs, recording the signal of Alexa488 fluorophores on the DNA origami. The custom-built script loads the micrograph, where the user identifies rough locations for three positions: i) the boundaries between lipid phases, and ii) a location of the L_d domain. Using these positions, a circle is fitted as reference so to enclose the membrane within a ring. Image processing proceeds with a first segmentation module, where a line connecting the two concentric circles (in red) is projected radially using polar coordinates. Thus, radial intensity profiles are acquired, from $\theta = 0$ to 2π in steps of $\pi/900$. From individual radial profiles, we extracted the location of the membrane *via* numerical integration around the membrane peak, as determined with a Gaussian fit. To further account for imperfect segmentation due to noise, these positions (shown in yellow in the middle micrograph) are filtered in a second segmentation module. The latter uses a subset of the membrane positions, namely those that are within $\pm 5\%$ of the estimated radius of the vesicle. These points are then subjected to a circle fitting routine for each lipid (quasi-hemispherical) domain, and the average membrane intensity values are extracted at a distance equal to the radius of the circle (in red and green in the right micrograph). These points are used to construct an intensity profile around the location of the line-interface, as described in Supplementary Note II. Scale bar = $10 \mu\text{m}$.

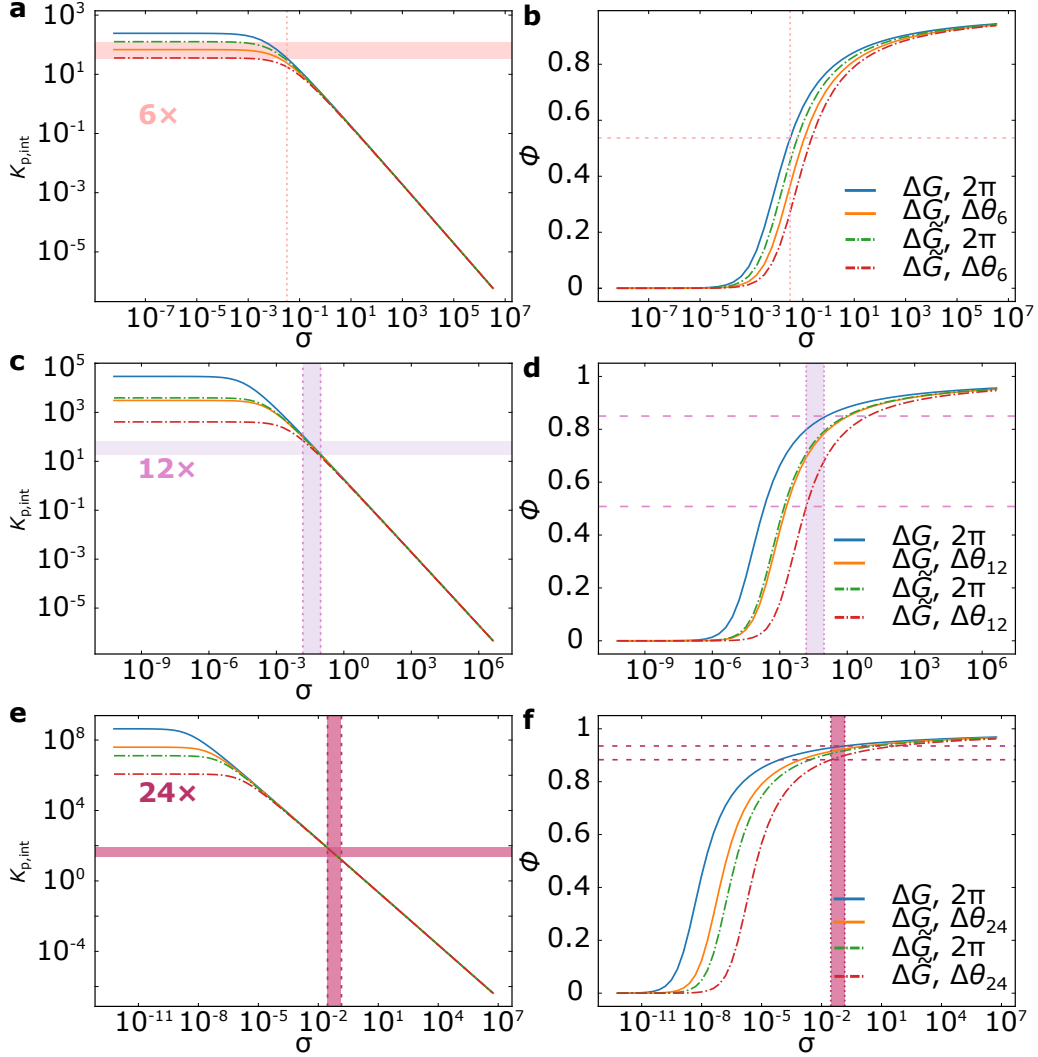


Figure S5: Comparing experimental trends with our numerical model reveals the regulatory effect on line-partitioning afforded by DNA nanostructures. **a–c** Plots of the partitioning coefficient ($K_{p,int}$) as a function of surface coverage (σ), computed using $\xi = 8\text{nm}$ and the parameter values compiled in Table S6 for: i) the free-energy contributions for partitioning assuming all anchor-points are present in the line-actant (ΔG , solid lines); or ii) the free-energy contributions for partitioning correcting for the probability of staple incorporation ($\Delta\tilde{G}$, dash-dot lines), as quantified by Jungmann and co-workers; iii) the reduced rotational freedom of the tiles upon accumulating at the line-interface due to the position of the anchor-points, which we describe with $\Delta\theta_n$ (orange/red curves); and finally iv) tiles with full rotational freedom ($\Delta\theta = 2\pi$, blue/green curves). By intersecting the experimental line-partitioning coefficients \pm standard deviation ($K_{p,int} \pm \delta K_{p,int}$, horizontal shaded region) with the curves from the theoretical predictions, we can infer surface coverages (σ) relevant to the scenarios outlined above (i–iv), providing us with a degree of uncertainty (vertical shaded region). **d–f** We then apply the inferred ranges of σ to estimate the fraction of occupied line-interface (ϕ), computed by solving Eq. S14 for scenarios i–iv, which provides us with lower and upper bounds for $\phi_{n\times}$. The resulting ranges of σ and ϕ are summarised in Fig. S6 and Fig. 2 (main text), respectively.

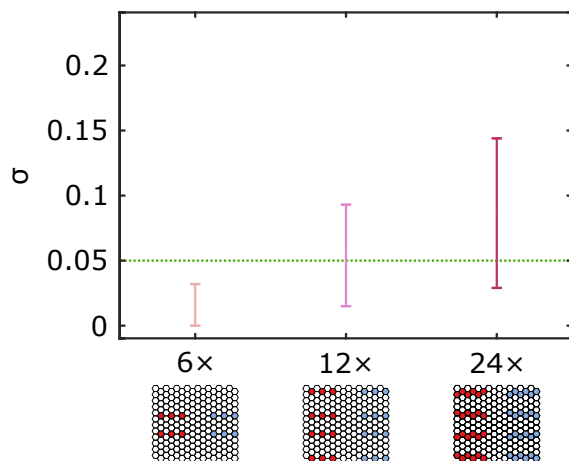


Figure S6: The predicted surface coverage is similar to the expected experimental value As discussed in Supplementary Note III, we inferred the surface coverage ($\sigma = \rho L_1 L_2$) of line-actants on membranes in view of their experimental line-partitioning tendencies (Fig. 2 in the main text and Supplementary Fig. S5). The estimated ranges of σ for each line-actant design is similar to the anticipated experimental values ($\sigma_{\text{exp}} \sim 0.05$, green dashed line). In the case of the 6x design, we observe ranges of surface coverage slightly below the nominal experimental value, which we ascribe to the lower membrane-affinity of the nanostructures given the fewer number of anchor-points they feature.

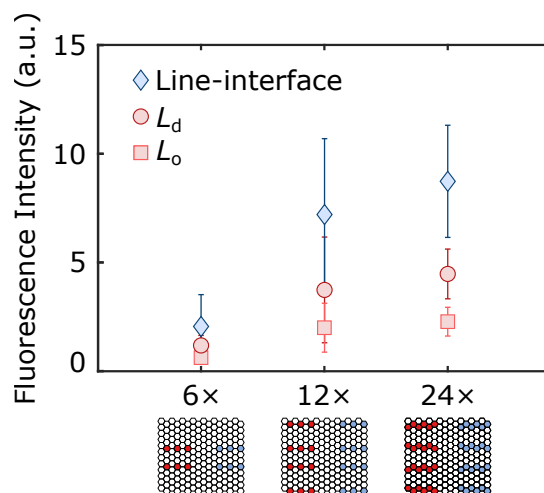


Figure S7: Lower number of anchors results in a lower surface density of line-actants. The absolute fluorescence intensities quantified from equatorial confocal micrographs show that nanostructures equipped with 6 \times have systematically lower membrane fluorescence intensities than those detected for GUVs decorated with 12 \times and 24 \times dC and sT anchor-points, thus suggesting lower surface densities. The latter can be due to an overall lower affinity of the nano-devices for the membrane.

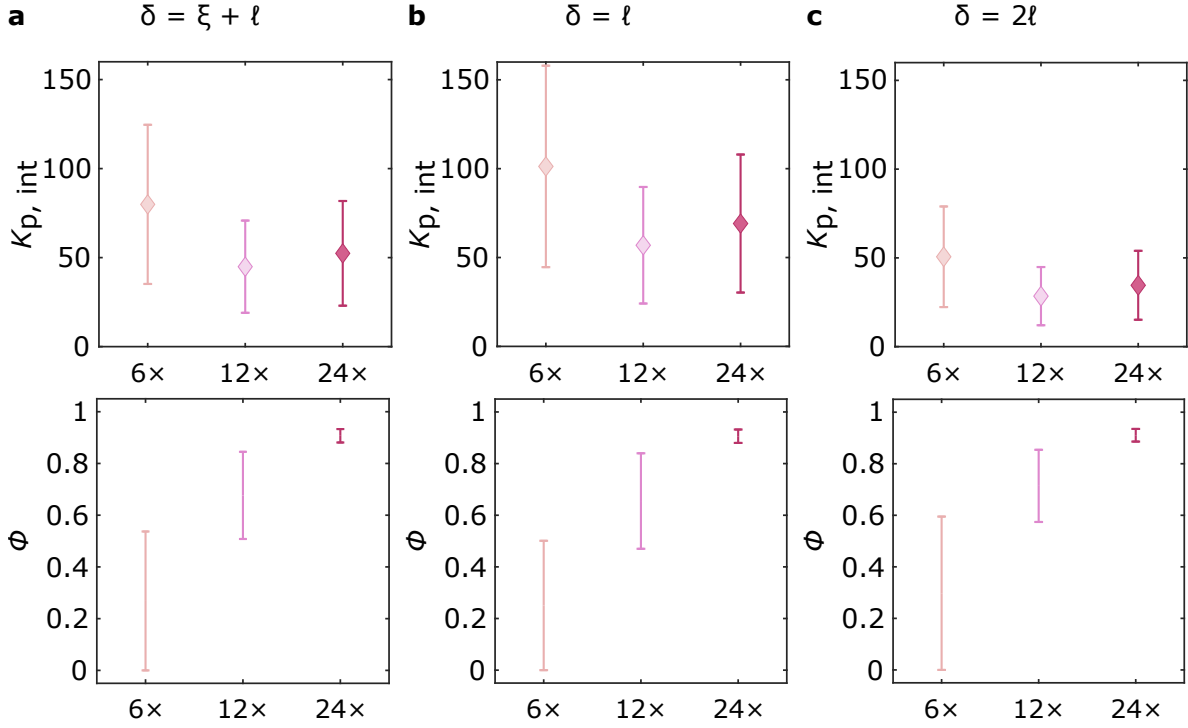


Figure S8: Error propagation of ξ to line-accumulation observables. The uncertainty on the estimation of ξ propagates to the values of $K_{p,int}$, while having a negligible influence on the estimation of ϕ . Comparing $\xi = 8$ nm (panel **a**) with both lower (panel **b**, $\xi = 0$) and upper (panel **c**, $\xi = 30$ nm, for $6\times$ and $12\times$ tiles, or $\xi = 25$ nm for $24\times$ tiles) physical bounds on the thickness of the line-interface shows that the values of $K_{p,int}$ shift slightly, and are all within a factor of two from each other. Conversely, the values of ϕ only negligibly change, and preserve the trend of increased line-accumulation with increasing number of anchor-points on the line-actants.

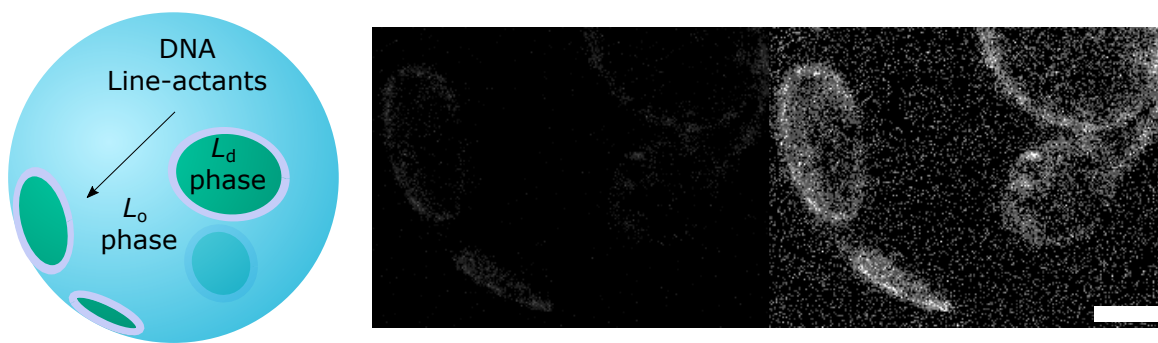


Figure S9: Line-active DNA nanostructures stabilise lipid domains by accumulating at line-interfaces. Line-accumulation of DNA nanostructures scaffolds lipid domains and renders them stable against coalescence, as shown with a 3D view of a reconstructed phase-separated vesicle after quenching below the miscibility transition temperature. Line-accumulation of fluorescent (Alexa488) DNA plates is readily noticeable, showing stable domains rendered from a confocal z-stack using Volume Viewer (FIJI³²) with (right) and without (left) contrast enhancement. Scale bar = 10 μm .

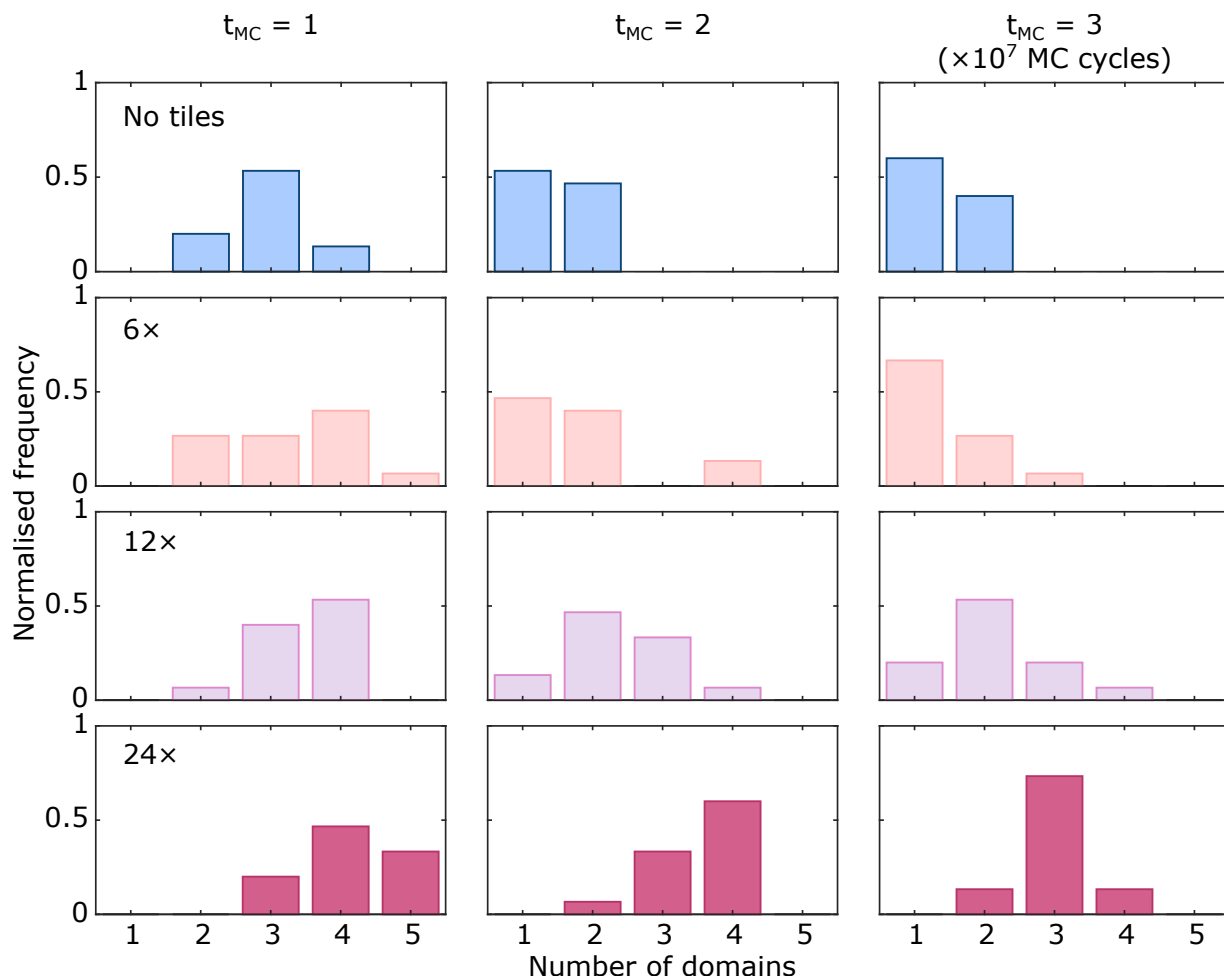


Figure S10: Time-evolution of domain stabilisation with line-active tiles. Frequency histograms comparing the number of domains in simulation runs, normalised to the total number of trajectories, at various t_{MC} in the presence of line-actant designs 6x ($n = 15$ trajectories), 12x ($n = 15$ trajectories), or 24x ($n = 15$ trajectories), comparing them to simulations run without DNA tiles ($n = 15$ trajectories).

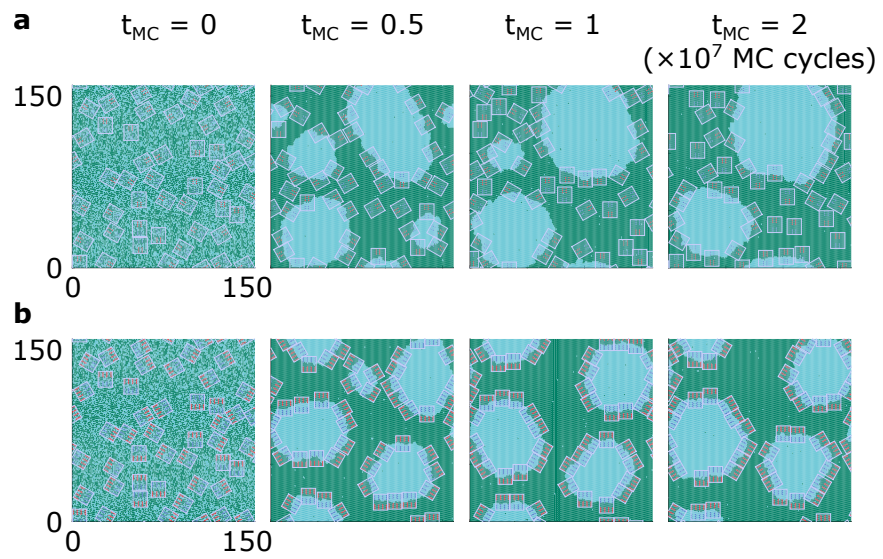


Figure S11: Temporal evolution of domain stabilisation with line-actant variants. Domain stabilisation demonstrated with representative snapshots at various t_{MC} for simulations with: **a** $6\times$ or **b** $24\times$ DOLAs.

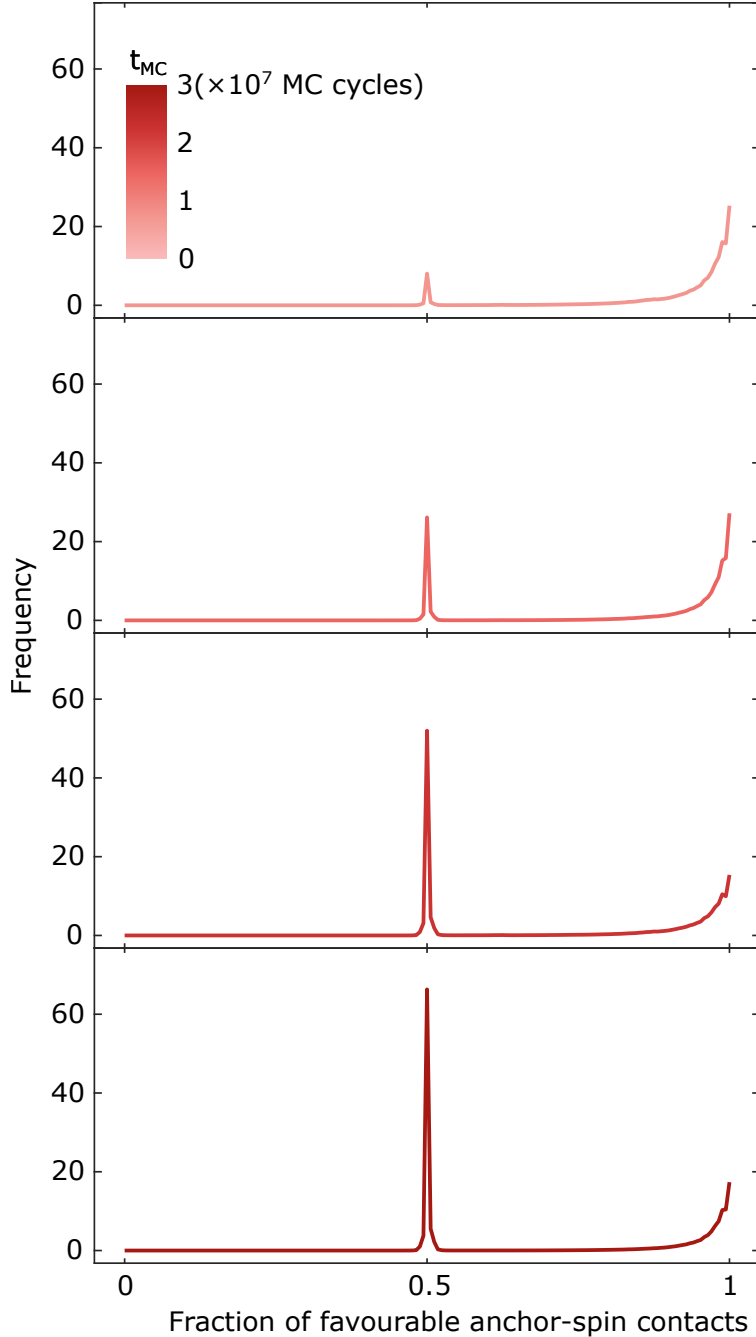


Figure S12: The fraction of favourable anchor-spin contacts are used to assess line-accumulation of DNA tiles. In order to compute the number of tiles adsorbed at the line-interface, we use the fraction of favourable anchor-spin contacts. A tile is said to be at the line when featuring at least 80% of favourable anchor-spin interactions relative to the total contacts. At early t_{MC} , when most tiles are adsorbed at the line-interface, we observe a high frequency of favourable anchor-spin contacts ~ 1 , with only few occurrences of 0.5 contacts. Late t_{MC} indicate line-interface minimisation and the associated translocation of the tiles from the interface to the green phase, which results in half of the anchor-points being hosted in their unfavourable phase. The latter thus shifts the frequencies of favourable anchor-spin contacts to 0.5, increasing the height of the peak.

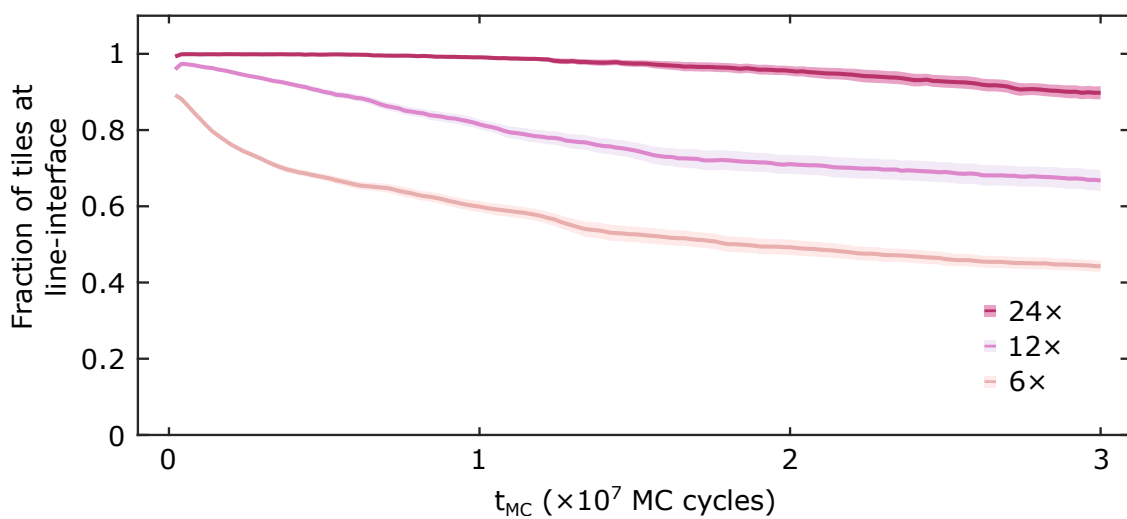


Figure S13: Domain coarsening drives tile desorption from line-interfaces. As the simulations progress, the fraction of tiles adsorbed at line-interfaces decreases to levels that increase monotonically with the number of anchor-points. Note that, even for the line-accumulating design with the most favourable free-energy gain (24×), there is still a substantial decrease, hinting at the prevalence of Ostwald ripening.

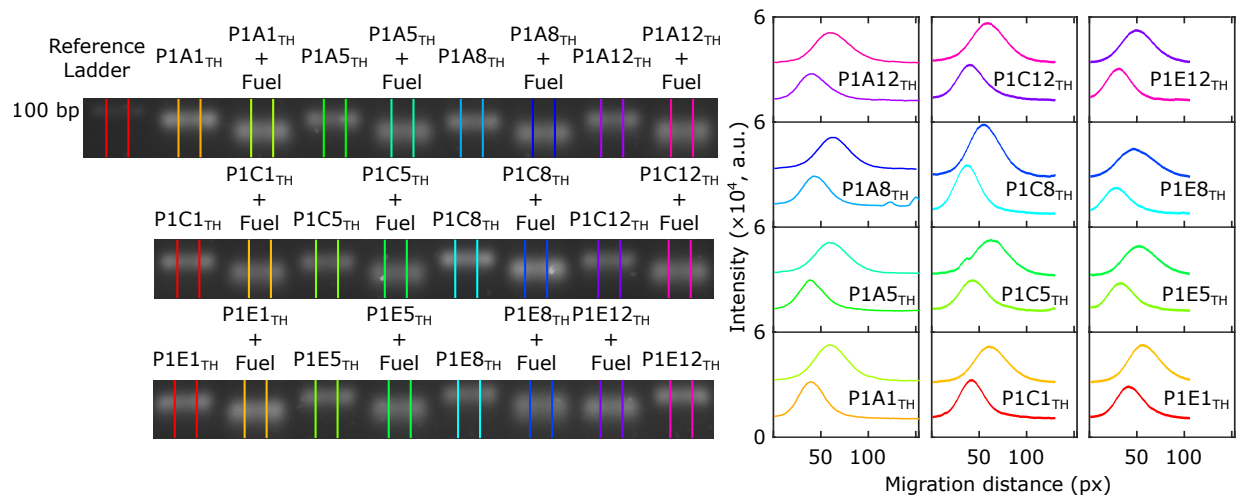


Figure S14: Reconfigurability of anchor-points through toehold reactions confirmed with AGE. Agarose gel electrophoresis demonstrates functionality of the toehold reaction in each (dC) anchor-point used for the dynamic line-actants in Fig. 5 and Fig. 6 in the main text. Each dC-targeting staple, bearing the toehold with sequence α , was assembled via annealing with their corresponding (non-cholesterolised) dC anchor module. Gel electrophoresis was run on these nanostructures, and also in the presence of Fuel, as indicated in each lane. The toehold reaction catalysed by the Fuel detaches the staple from the anchor-modules, resulting in smaller constructs and thus different migration profiles. The shift and broadening of the peaks after the addition of Fuel in the intensity profiles are indicative of construct reconfiguration into smaller devices, thus confirming the molecular response for each staple.

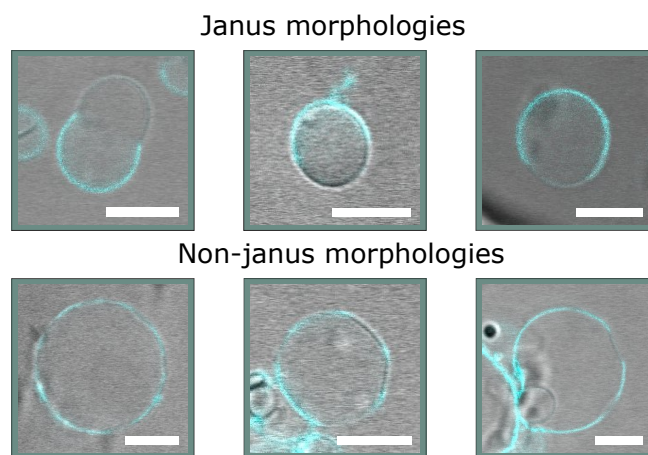


Figure S15: Changes in spontaneous curvature in GUVs can stabilise lipid domains. Confocal micrograph overlays showing representative examples of Janus-looking line-actant functionalised GUVs, after a heating-cooling program and exposed to Fuel, co-existing with vesicles that still feature Non-janus morphologies. In the latter case, it is noticeable that the spontaneous curvature of the vesicle has deviated from that of a sphere, likely due to small osmotic imbalances due to the addition of Fuel, which allowed lipid domains to retain stability against coalescence. In cyan, the fluorescent signal of the DOLAs, fluorescently labelled with Alexa488. All scale bars = $10\ \mu\text{m}$.

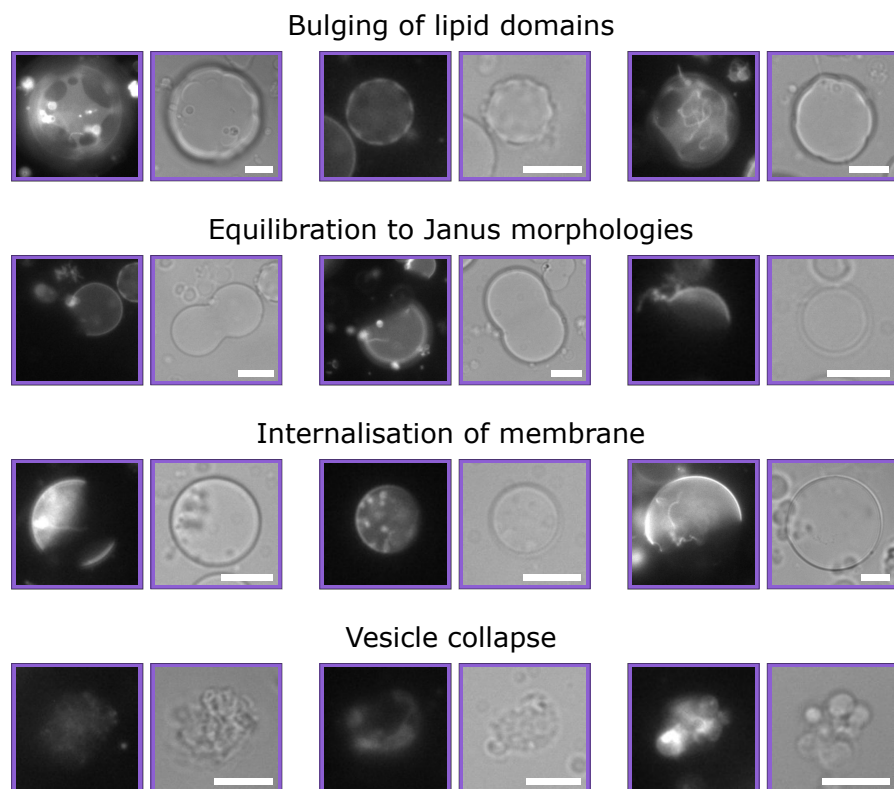


Figure S16: Influence of hyperosmosis in GUVs. Inducing hyperosmosis at $C_O/C_I \approx 1.28$ leads to sample heterogeneity across vesicles. We observed four possible outcomes in hyperosmolar conditions: i) bulging of line-actant stabilised lipid domains; ii) equilibration to Janus-like morphologies; iii) uptake of membrane to reduce the excess surface area, leading to taut vesicles, and; iv) vesicle collapse, likely due to the fast changes in osmotic conditions. All scale bars = $10 \mu\text{m}$.

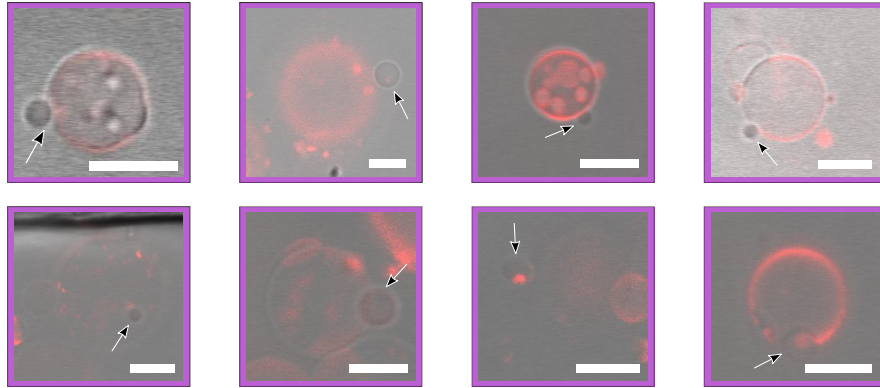


Figure S17: Fission in line-actant functionalised liposomes. Confocal micrograph overlays of domain fission events, including those in Fig. 6 in the main text, where GUVs featuring DOLAs were exposed to hyperosmotic shock ($C_O/C_I \approx 1.28$) and supplemented with Fuel to trigger line-actant reconfiguration. Vesicles immersed in buffer with Fuel mostly featured the expected Janus-like morphologies, suggesting domain coarsening. In these conditions, we identified a further 7 events, shown with representative examples here alongside those included in Fig. 6, indicating that fission occurred in some synthetic cells, while other vesicles fully relaxed into Janus morphologies. Both the competition between line energy and fluctuation entropy as well as the kinetics of toehold-induced domain re-organisation could account for sample heterogeneity. Specifically, unlike measurements in Fig. 5, the progression of strand displacement is not limited by the diffusion of Fuel molecules and may occur in timescales comparable to those of osmosis, which could in some instances lead to equilibration to single-domain phases prior to domain budding, at which point fission can no longer proceed. The red signal detected is that of TexasRed-DHPE, which stains the L_d phase. All scale bars = $10 \mu\text{m}$.

Supplementary Movies Key

Supplementary Movie 1: Representative simulation trajectory with $12 \times$ DNA-origami Line-actants following the system after quenching for 2×10^7 MC cycles. Box size: 320×372 lattice points.

Supplementary Movie 2: Representative simulation trajectory with $12 \times$ DNA-origami Line-actants following the system after quenching for 3×10^7 MC cycles. Box size: 160×172 lattice points.

Supplementary Movie 3: Representative simulation trajectory lacking DNA-origami Line-actants following the system after quenching for 3×10^7 MC cycles. Box size: 160×172 lattice points.

Supplementary Movie 4: Representative simulation trajectory with $24 \times$ DNA-origami Line-actants following the system after quenching for 3×10^7 MC cycles. Box size: 160×172 lattice points.

Supplementary Movie 5: Representative simulation trajectory with $6 \times$ DNA-origami Line-actants following the system after quenching for 3×10^7 MC cycles. Box size: 160×172 lattice points.

Supplementary Movie 6: Evolution of L_o -domain fission event in a representative vesicle observed with brightfield and epi-fluorescence microscopy. Time-stamps refer to the time elapsed after initial acquisition. Fuel was added 2 minutes before acquisition began. The fluorescent marker is TexasRed-DHPE, which labels the L_d phase. Scale bar: $10 \mu\text{m}$.

Supplementary Movie 7: Evolution of L_o -domain fission event in a representative

vesicle observed with overlaid confocal and brightfield microscopy. Time-stamps refer to the time elapsed after initial acquisition. Fuel was added 90 minutes before acquisition began. The fluorescent marker is TexasRed-DHPE, which labels the L_d phase. Scale bar: 10 μm .

Supplementary Tables

Table S1: **Staple sequences for DNA origami tile.** Sequences of oligonucleotides comprising the origami plate, highlighting in **bold** the overhangs extended in selected staples to accommodate domains to bind anchor-modules dC (blue) and sT (red) as well as the fluorescent beacon $\text{Lin}^{\text{f},*}$ or Extender- $3\times\text{Lin}^{\text{f},*}$ (green).

Name	Sequence
P1A01	TTTTCACTCAAAGGGCGAAAAACCATCACCG GGTTTGTGTTGTGTTGG
P1A02	GTCGACTTCGGCCAACGCGCGGGGTTTTTC
P1A03	TGCATCTTTCCCAGTCACGACGGCTGCAG
P1A04	TAATCAGCGGATTGACCGTAATCGTAACCG
P1A05	AACGCAAAATCGATGAACGGTACCGGTTGA GGTTTGTGTTGTGTTGG
P1A06	AACAGTTTTGTACCAAAAACATTTTATTTTC
P1A07	TTTACCCCAACATGTTTTAAATTTCCATAT
P1A08	TTTAGGACAAATGCTTTAAACAATCAGGTC GGTTTGTGTTGTGTTGG
P1A09	CATCAAGTAAAACGAACCTAACGAGTTGAGA
P1A10	AATACGTTTGAAAGAGGACAGACTGACCTT
P1A11	AGGCTCCAGAGGCTTTGAGGACACGGGTAA
P1A12	AGAAAGGAACAACCTAAAGGAATTCAAAAAA GGTTTGTGTTGTGTTGG
P1B01	CAAATCAAGTTTTTTGGGGTCGAAACGTGGA GGTTTGTGTTGTGTTGG
P1B02	CTCCAACGCAGTGAGACGGGCAACCAGCTGCA
P1B03	TTAATGAACTAGAGGATCCCCGGGGGTAACG
P1B04	CCAGGGTTGCCAGTTTGAGGGGACCCGTGGGA GGTTTGTGTTGTGTTGG
P1B05	ACAAACGGAAAAGCCCCAAAAACACTGGAGCA
P1B06	AACAAGAGGGATAAAAATTTTTAGCATAAAGC
P1B07	TAAATCGGGATTCCCAATTCTGCGATATAATG
P1B08	CTGTAGCTTGACTATTATAGTCAGTTCATTGA GGTTTGTGTTGTGTTGG
P1B09	ATCCCCCTATAACCACATTCAACTAGAAAAATC
P1B10	TACGTTAAAGTAATCTTGACAAGAACCGAACT
P1B11	GACCAACTAATGCCACTACGAAGGGGTAGCA GGTTTGTGTTGTGTTGG
P1B12	ACGGCTACAAAAGGAGCCTTTAATGTGAGAAT
P1C01	AGCTGATTGCCCTTCAGAGTCCACTATTAAAGGGTGCCGT GGTTTGTGTTGTGTTGG
P1C04	GTATAAGCCAACCCGTCCGATTCTGACGACAGTATCGGCCGCAAGGCG
P1C05	TATATTTTGTCAATTGCCTGAGAGTGGAAGATT GGTTTGTGTTGTGTTGG
P1C06	GATTTAGTCAATAAAGCCTCAGAGAACCCTCA
P1C07	CGGATTGCAGAGCTTAATTGCTGAAACGAGTA
P1C08	ATGCAGATACATAACGGGAATCGTCATAAATAAAGCAAAG GGTTTGTGTTGTGTTGG
P1C11	TTTATCAGGACAGCATCGGAACGACACCAACCTAAAACGAGGTCAATC
P1C12	ACAACCTTCAACAGTTTCAGCGGATGTATCGG GGTTTGTGTTGTGTTGG
P1D01	AAAGCACTAAATCGGAACCCTAATCCAGTT GGTTTGTGTTGTGTTGG

P1D02	TGGAACAACCGCCTGGCCCTGAGGCCCGCT
P1D03	TTCCAGTCGTAATCATGGTCATAAAAGGGG
P1D04	GATGTGCTTCAGGAAGATCGCACAATGTGA GGTTTGGTTGTTGTGTTGG
P1D05	GCGAGTAAAAATATTTAAATTTGTTACAAAG
P1D06	GCTATCAGAAATGCAATGCCTGAATTAGCA
P1D07	AAATTAAGTTGACCATTAGATACTTTTGCG
P1D08	GATGGCTTATCAAAAAGATTAAGAGCGTCC GGTTTGGTTGTTGTGTTGG
P1D09	AATACTGCCAAAAGGAATTACGTGGCTCA
P1D10	TTATAACCAAAATCAACGTAACGAACGAG
P1D11	GCGCAGACAAGAGGCAAAAAGAATCCCTCAG GGTTTGGTTGTTGTGTTGG
P1D12	CAGCGAAACTTGCTTTTCGAGGTGTTGCTAA
P1E01	AGCAAGCGTAGGGTTGAGTGTGTAGGGAGCC GGTTTGGTTGTTGTGTTGG
P1E02	CTGTGTGATTGCGTTGCGCTCACTAGAGTTGC
P1E03	GCTTTCGATTACGCCAGCTGGCGGCTGTTTC
P1E04	ATATTTTGGCTTTCATCAACATTATCCAGCCA
P1E05	TAGGTAAACTATTTTGGAGAGATCAAACGTTA GGTTTGGTTGTTGTGTTGG
P1E06	AATGGTCAACAGGCAAGGCAAAGAGTAATGTG
P1E07	CGAAAGACTTTGATAAGAGGTCATATTTGCA
P1E08	TAAGAGCAAATGTTTAGACTGGATAGGAAGCC GGTTTGGTTGTTGTGTTGG
P1E09	TCATTCAGATGCGATTTTAAGAACAGGCATAG
P1E10	ACACTCATCCATGTTACTTAGCCGAAAGCTGC
P1E11	AAACAGCTTTTTGCGGGATCGTCAACACTAAA
P1E12	TAAATGAATTTTCTGTATGGGATTAATTTCTT GGTTTGGTTGTTGTGTTGG
P1F01	CCCGATTTAGAGCTTGACGGGGAAAAAGAATA GGTTTGGTTGTTGTGTTGG
P1F02	GCCCGAGAGTCCACGCTGGTTTGCAGCTAACT
P1F03	CACATTA AAATGTTATCCGCTCATGCGGGCC
P1F04	TCTTCGCTGCACCGCTTCTGGTGCGGCCTTCC GGTTTGGTTGTTGTGTTGG
P1F05	TGTAGCCATTAAAATTCGCATTAAATGCCGGA
P1F06	GAGGGTAGGATTCAAAGGGTGAGACATCCAA
P1F07	TAAATCATATAACCTGTTTAGCTAACCTTTAA
P1F08	TTGCTCCTTTCAAATATCGCGTTTGAGGGGGT GGTTTGGTTGTTGTGTTGG
P1F09	AATAGTAAACACTATCATAACCCCTCATTGTGA
P1F10	ATTACCTTTGAATAAGGCTTGCCCAAATCCGC
P1F11	GACCTGCTCTTTGACCCCCAGCGAGGGAGTTA GGTTTGGTTGTTGTGTTGG
P1F12	AAGCCGCTGATACCGATAGTTGCGACGTTAG
P1G01	CCCAGCAGGCGAAAAATCCCTTATAAATCAAGCCGGCG
P1G04	TAAATCAAATAATTCGCGTCTCGGAAACCAGGCAAAGGGAAGG
P1G05	GAGACAGCTAGCTGATAAATTAATTTTTGT
P1G06	TTGGGGATAGTAGTAGCATTAAAAGGCCG
P1G07	GCTTCAATCAGGATTAGAGAGTTATTTTCA
P1G08	CGTTTACCAGACGACAAAAGAAGTTTTGCCATAATTCGA

P1G11	TGACAACCTCGCTGAGGCTTGCATTATACCAAGCGCGATGATAAA
P1G12	TCTAAAGTTTTGTCGTCTTTCCAGCCGACAA
P1H01	TCAATATCGAACCTCAAATATCAATTCCGAAA
P1H02	GCAATTCACATATTCCTGATTATCAAAGTGTA
P1H03	AGAAAACAAAGAAGATGATGAAACAGGCTGCG
P1H04	ATCGCAAGTATGTAAATGCTGATGATAGGAAC
P1H05	GTAATAAGTTAGGCAGAGGCATTTATGATATT
P1H06	CCAATAGCTCATCGTAGGAATCATGGCATCAA
P1H07	AGAGAGAAAAAATGAAAAATAGCAAGCAAACCT
P1H08	TTATTACGAAGAAGCTGGCATGATTGCGAGAGG
P1H09	GCAAGGCCTCACCAGTAGCACCATGGGCTTGA
P1H10	TTGACAGGCCACCACCAGAGCCGCGATTTGTA
P1H11	TTAGGATTGGCTGAGACTCCTCAATAACCGAT
P1H12	TCCACAGACAGCCCTCATAGTTAGCGTAACGA
P2A01	AACGTGGCGAGAAAGGAAGGGAAACCAGTAA
P2A02	TCGGCAAATCCTGTTTGATGGTGGACCCTCAA
P2A03	AAGCCTGGTACGAGCCGGAAGCATAGATGATG
P2A04	CAACTGTTGCGCCATTTCGCCATTCAAACATCA
P2A05	GCCATCAAGCTCATTTTTTAACCACAAATCCA
P2A06	CAACCGTTTCAAATCACCATCAATTCGAGCCA
P2A07	TTCTACTACGCGAGCTGAAAAGGTTACCGCGC
P2A08	CCAACAGGAGCGAACCAGACCCGGAGCCTTTAC
P2A09	CTTTTGCAGATAAAAACCAAATAAAGACTCC
P2A10	GATGGTTTGAACGAGTAGTAAATTTACCATTA
P2A11	TCATCGCCAACAAAGTACAACGGACGCCAGCA
P2A12	ATATTCGGAACCATCGCCCACGCAGAGAAGGA
P2B01	TAAAAGGGACATTCTGGCCAACAAAGCATC
P2B02	ACCTTGCTTGGTCAGTTGGCAAAGAGCGGA
P2B03	ATTATCATTCAATATAATCCTGACAATTAC
P2B04	CTGAGCAAAAATTAATTACATTTTGGGTTA
P2B05	TATAACTAACAAGAACGCGAGAACGCCAA
P2B06	CATGTAATAGAAATATAAAGTACCAAGCCGT
P2B07	TTTTATTTAAGCAAATCAGATATTTTTTGT
P2B08	TTAACGTCTAACATAAAAACAGGTAACGGA
P2B09	ATACCCAACAGTATGTTAGCAAATTAGAGC
P2B10	CAGCAAAAGGAAACGTCACCAATGAGCCGC
P2B11	CACCAGAAAGGTTGAGGCAGGTCATGAAAG
P2B12	TATTAAGAAGCGGGGTTTTGCTCGTAGCAT
P2C01	TCAACAGTTGAAAGGAGCAAATGAAAAATCTAGAGATAGAG GGTGTAGTTAATGGGAGT
P2C02	XXXXXXXXXXXXXXXXXX ATTAAGTTTACCAGCTCGAATTCGGGAAACCTGTCTGTC
P2C03	XXXXXXXXXXXXXXXXXX ATAAGGGAACCGGATATTCATTACGTCAGGACGTTGGGAA

P2C04	TCAAATATAACCTCCGGCTTAGGTAACAATTTTCATTTGAAGGCGAATT
P2C05	GTAAAGTAATCGCCATATTTAACAAAACTTTT GGTGTAGTTAATGGGAGT
P2C06	TATCCGGTCTCATCGAGAACAAGCGACAAAAG
P2C07	TTAGACGGCCAAATAAGAAACGATAGAAGGCT
P2C08	CGTAGAAAATACATACCGAGGAAACGCAATAAGAAGCGCA GGTGTAGTTAATGGGAGT
P2C09	XXXXXXXXXXXXXXXXXX GCGATCGGCAATTCACACAACAGGTGCCTAATGAGTG
P2C10	XXXXXXXXXXXXXXXXXX TTGTGTCGTGACGAGAAACACCAAATTTCAACTTTAAT
P2C11	GCGGATAACCTATTATTCTGAAACAGACGATTGGCCTTGAAGAGCCAC
P2C12	TCACCGTACAACTACAACGCCTAGTACCAG GGTGTAGTTAATGGGAGT
P2D01	ACCCCTCTGACCTGAAAGCGTAAGACGCTGAG GGTGTAGTTAATGGGAGT
P2D02	AGCCAGCAATTGAGGAAGGTTATCATCATTTTT
P2D03	GCGGAACATCTGAATAATGGAAGGTACAAAAT
P2D04	CGCGCAGATTACCTTTTTTAATGGGAGAGACT GGTGTAGTTAATGGGAGT
P2D05	ACCTTTTTATTTTAGTTAATTTTCATAGGGCTT
P2D06	AATTGAGAATTCTGTCCAGACGACTAAACCAA
P2D07	GTACCGCAATTCTAAGAACGCGAGTATTATTT
P2D08	ATCCCAATGAGAATTAACCTGAACAGTTACCAG GGTGTAGTTAATGGGAGT
P2D09	AAGGAAACATAAAGGTGGCAACATTATCACCG
P2D10	TCACCGACGCACCGTAATCAGTAGCAGAACCG
P2D11	CCACCCCTCTATTCACAAACAAATACCTGCCTA GGTGTAGTTAATGGGAGT
P2D12	TTTCGGAAGTGCCGTCGAGAGGGTGAGTTTCG
P2E01	CTTTAGGGCCTGCAACAGTGCCAATACGTG GGTGTAGTTAATGGGAGT
P2E02	CTACCATAGTTTGAGTAACATTTAAAATAT
P2E03	CATAAATCTTTGAATACCAAGTGTTAGAAC
P2E04	CCTAAATCAAAATCATAGGTCTAAACAGTA
P2E05	ACAACATGCCAACGCTCAACAGTCTTCTGA GGTGTAGTTAATGGGAGT
P2E06	GCGAACCTCCAAGAACGGGTATGACAATAA
P2E07	AAAGTCACAAAATAAACAGCCAGCGTTTTA
P2E08	AACGCAAAGATAGCCGAACAAACCTGAAC GGTGTAGTTAATGGGAGT
P2E09	TCAAGTTTCATTAAAGGTGAATATAAAAAGA
P2E10	TTAAAGCCAGAGCCGCCACCCTCGACAGAA
P2E11	GTATAGCAAACAGTTAATGCCCAATCCTCA
P2E12	AGGAACCCATGTACCGTAACACTTGATATAA GGTGTAGTTAATGGGAGT
P2F01	GCACAGACAATATTTTTGAATGGGGTCAGTA GGTGTAGTTAATGGGAGT
P2F02	TTAACACCAGCACTAACAACCTAATCGTTATTA
P2F03	ATTTTAAAATCAAAATTATTTGCACGGATTTCG
P2F04	CCTGATTGCAATATATGTGAGTGATCAATAGT GGTGTAGTTAATGGGAGT
P2F05	GAATTTATTTAATGGTTTGAAATATTCTTACC
P2F06	AGTATAAAGTTCAGCTAATGCAGATGTCTTTC
P2F07	CTTATCATTTCCCGACTTGCGGGAGCCTAATTT
P2F08	GCCAGTTAGAGGGTAATTGAGCGCTTTAAGAA GGTGTAGTTAATGGGAGT

P2F09	AAGTAAGCAGACACCACGGAATAATATTGACG
P2F10	GAAATTATTGCCTTTAGCGTCAGACCGGAACC
P2F11	GCCTCCCTCAGAATGGAAAGCGCAGTAACAGT GGTGTAGTTAATGGGAGT
P2F12	GCCCGTATCCGGAATAGGTGTATCAGCCCAAT
P2G01	AGATTAGAGCCGTCAAAAAACAGAGGTGAGGCCTATTAGT GGTGTAGTTAATGGGAGT
P2G02	XXXXXXXXXXXXXXXXXX ATTTCATTTTTGTTTTGGATTATACTAAGAAACCACCAGAAG
P2G03	XXXXXXXXXXXXXXXXXX CACCCTCAGAAACCATCGATAGCATTGAGCCATTTGGGAA
P2G04	GTGATAAAAAGACGCTGAGAAGAGATAACCTTGCTTCTGTTCCGGGAGA
P2G05	GTTTATCAATATGCGTTATACAAAACCGACCGT GGTGTAGTTAATGGGAGT
P2G06	GCCTTAAACCAATCAATAATCGGCACGCGCT
P2G07	GAGAGATAGAGCGTCTTTCCAGAGTTTTGAA
P2G08	GTTTATTTTGTCCACAATCTTACCGAAGCCCTTTAATATCA GGTGTAGTTAATGGGAGT
P2G09	XXXXXXXXXXXXXXXXXX AACAATAACGTAAAACAGAAATAAAAATCCTTTGCCCGAA
P2G10	XXXXXXXXXXXXXXXXXX AGCCACCCTGTAGCGGTTTTCAAGGGAGGGAAGGTAAA
P2G11	CAGGAGGTGGGGTCAGTGCCTTGAGTCTCTGAATTTACCGGGAACCAG
P2G12	CCACCCTCATTTTCAGGGATAGCAACCGTACT GGTGTAGTTAATGGGAGT
P2H01	CTTTAATGCGCGAACTGATAGCCCCACCAG GGTGTAGTTAATGGGAGT
P2H02	CAGAAGATTAGATAATACATTTGTCGACAA
P2H03	CTCGTATTAGAAATTGCGTAGATACAGTAC
P2H04	CTTTTACAAAATCGTCGCTATTAGCGATAG GGTGTAGTTAATGGGAGT
P2H05	CTTAGATTTAAGCGTTAAATAAAGCCTGT
P2H06	TTAGTATCACAAATAGATAAGTCCACGAGCA
P2H07	TGTAGAAATCAAGATTAGTTGCTCTTACCA
P2H08	ACGCTAACCCACAAGAATTGAAAATAGC GGTGTAGTTAATGGGAGT
P2H09	AATAGCTATCAATAGAAAATTCAACATTCA
P2H10	ACCGATTGTCGGCATTTCGGTCATAATCA
P2H11	AAATCACCTTCCAGTAAGCGTCAGTAATAA GGTGTAGTTAATGGGAGT
P2H12	GTTTTAACTTAGTACCGCCACCCAGAGCCA

Table S2: **Staples for each line-actant design to achieve line-accumulation:** Selected staples that feature an added overhang as an anchor-point in each variant of our line-actants.

6×		12×		24×	
dC	sT	dC	sT	dC	sT
P1A5	P2C5	P1A1	P2C1	P1A1	P2C1
P1A8	P2C8	P1A5	P2C5	P1A5	P2C5
P1C5	P2E1	P1A8	P2C8	P1A8	P2C8
P1C8	P2E5	P1A12	P2C12	P1A12	P2C12
P1E5	P2G5	P1C1	P2E1	P1B1	P2D1
P1E8	P2G8	P1C5	P2E5	P1B4	P2D4
		P1C8	P2E8	P1B8	P2D8
		P1C12	P2E12	P1B11	P2D11
		P1E1	P2G1	P1C1	P2E1
		P1E5	P2G5	P1C5	P2E5
		P1E8	P2G8	P1C8	P2E8
		P1E12	P2G12	P1C12	P2E12
				P1D1	P2F1
				P1D4	P2F4
				P1D8	P2F8
				P1D11	P2F11
				P1E1	P2G1
				P1E5	P2G5
				P1E8	P2G8
				P1E12	P2G12
				P1F1	P2H1
				P1F4	P2H4
				P1F8	P2H8
				P1F11	P2H11

Table S3: **Anchor modules and oligonucleotides that comprise them.** Each construct is self-assembled through a quenching temperature ramp as discussed in the Methods at a final concentration of $2\ \mu\text{M}$ and then diluted for GUV functionalisation. Constructs require strands in 1:1 stoichiometric ratios.

Construct	Strands
Anchor _{dC}	C _{bb,chol} + C _{b,chol}
Anchor _{sT}	E _{bb} + E _{b,toc}

Table S4: **Sequences of oligonucleotide strands.** Abbreviations: TEG: triethyleneglycol.

Strand	Sequence (5' → 3')
C _{b,chol}	/Cholesteryl-TEG/CAATCACACCACAAACACCCAACACAACAACAAACC
C _{bb,chol}	GTGTTTGTGGTGTGATTG/Cholesterol-TEG/
E _{bb}	CGCACTCTCACGCTAAAC
E _{b,toc}	/Octyl-Tocopherol/GTTTAGCGTGAGAGTGCGACTCCCATTAACTACACC
Lin ^{f,*}	GCTCTCTCATCACTAC/AlexaFluor488/
Extender	GTGTTGAGTAGTGAGATGGTAGTGATGAGAGAGCGTAGTGATGAGAGAGCGTAGT GATGAGAGAGC

Table S5: **Sequences of domains added to staples for fluorescent beacon hybridisation.** Docking domains were added replacing the domains marked as **XXXXXXXXXXXXXXXXXX**. Note that the extended beacon requires a stoichiometric mixture of Extender + (3×)Lin^{f,*}.

Strand	Sequence (5' → 3')
Docking _{Lin^f}	GTAGTGATGAGAGAGC
Docking _{Extender}	CATCTCACTACTCAACAC

Table S6: **Parameters and values for numerical model.** The table lists the parameters that have been used to infer the density of tiles at the line from the experimental values of the line-partitioning $K_{p,int}^{\times n}$ ($n = 6, 12,$ and 24). See Supplementary Discussion III for the definitions of the parameters.

Tiles	$K_{p,int}^{\times n}$	$\delta K_{p,int}^{\times n}$	$\beta\Delta G_{P,L_d}$	$\beta\Delta G_{P,L_o}$	$\beta\Delta\tilde{G}_{P,L_o}$	$\beta\Delta G_{p,int}$	$\beta\Delta\tilde{G}_{p,int}$	δ [nm]	L_1 [nm]	L_2 [nm]	$\Delta\theta$ [deg $^\circ$]
6 \times	79.9	44.7	0	6.6	5.91	-4.8	-4.15	38	75	80	101.3
12 \times	44.9	25.9	0	13.2	11.26	-9.6	-7.58	38	75	80	37.5
24 \times	52.4	29.4	0	26.4	21.42	-19.2	-15.68	33	75	80	32.6

Table S7: **Staple incorporation probabilities.** The table lists the Staple incorporation probabilities (p) used to compute Eq. S17. The values of p were reported by Jungmann and co-workers¹⁷ (see Supplementary Figure 14(b) in reference¹⁷)

dC		sT	
Staple	p	Staple	p
P1A12	0.699	P2C12	0.823
P1A8	0.914	P2C8	0.855
P1A5	0.85	P2C5	0.903
P1A11	0.602	P2C1	0.704
P1B11	0.833	P2D11	0.914
P1B8	0.85	P2D8	0.876
P1B4	0.769	P2D4	0.855
P1B1	0.774	P2D1	0.79
P1C12	0.737	P2E12	0.833
P1C8	0.821	P2E8	0.952
P1C5	0.79	P2E5	0.946
P1C1	0.667	P2E1	0.785
P1D11	0.882	P2F11	0.812
P1D8	0.941	P2F8	0.828
P1D4	0.871	P2F4	0.86
P1D1	0.871	P2F1	0.715
P1E12	0.753	P2G12	0.764
P1E8	0.925	P2G8	0.823
P1E5	0.882	P2G5	0.812
P1E1	0.839	P2G1	0.715
P1F11	0.86	P2H11	0.871
P1F8	0.893	P2H8	0.785
P1F4	0.833	P2H4	0.823
P1F1	0.742	P2H1	0.479

Table S8: **Average probability of staple incorporation p for dC and sT sets of anchor-points.** Average probabilities are computed from values in Table S7 for each line-actant design (see Table S4). In all cases, average probabilities for either set of anchor-points are $p \sim 0.8$, suggesting that an unbalance between anchor-modules on the tiles is unlikely.

Tile design	6×	12×	24×
Average p for dC	0.863	0.795	0.817
Average p for sT	0.854	0.826	0.813

Table S9: **Sequence of toehold domain and Fuel strand.** Toehold domains were added at the 3' termini of dC staples P1XX_{TH}

Strand	Sequence (5' → 3')
Toehold (α)	GTTGTA
Fuel	TACAACCCAACACAACAACAAACC

References

- (1) Angelova, M. I.; Dimitrov, D. S. Liposome electroformation. *Faraday Discuss. Chem. Soc.* **1986**, *81*, 303–311.
- (2) Veatch, S. L.; Keller, S. L. Separation of Liquid Phases in Giant Vesicles of Ternary Mixtures of Phospholipids and Cholesterol. *Biophys. J.* **2003**, *85*, 3074–3083.
- (3) Rubio-Sánchez, R.; Barker, S. E.; Walczak, M.; Cicuta, P.; Di Michele, L. A Modular, Dynamic, DNA-Based Platform for Regulating Cargo Distribution and Transport between Lipid Domains. *Nano Lett.* **2021**, *21*, 2800–2808.
- (4) Zadeh, J. N.; Steenberg, C. D.; Bois, J. S.; Wolfe, B. R.; Pierce, M. B.; Khan, A. R.; Dirks, R. M.; Pierce, N. A. NUPACK: Analysis and design of nucleic acid systems. *J. Comput. Chem.* **2010**, *32*, 170–173.
- (5) Kaufhold, W. T.; Brady, R. A.; Tuffnell, J. M.; Cicuta, P.; Di Michele, L. Membrane Scaffolds Enhance the Responsiveness and Stability of DNA-Based Sensing Circuits. *Bioconjug. Chem.* **2019**, *30*, 1850–1859.
- (6) Rothemund, P. W. K. Folding DNA to create nanoscale shapes and patterns. *Nature* **2006**, *440*, 297.
- (7) Schnitzbauer, J.; Strauss, M. T.; Schlichthaerle, T.; Schueder, F.; Jungmann, R. Super-resolution microscopy with DNA-PAINT. *Nat. Protoc.* **2017**, *12*, 1198–1228.
- (8) Stahl, E.; Martin, T. G.; Praetorius, F.; Dietz, H. Facile and Scalable Preparation of Pure and Dense DNA Origami Solutions. *Angew. Chem. Int. Ed* **2014**, *53*, 12735–12740.
- (9) Morzy, D.; Rubio-Sánchez, R.; Joshi, H.; Aksimentiev, A.; Di Michele, L.; Keyser, U. F. Cations regulate membrane-attachment and functionality of DNA nanostructures. *J. Am. Chem. Soc.* **2021**, *143*, 7358–7367.

- (10) Amjad, O. A.; Mognetti, B. M.; Cicuta, P.; Di Michele, L. Membrane Adhesion through Bridging by Multimeric Ligands. *Langmuir* **2017**, *33*, 1139–1146.
- (11) Talbot, E. L.; Parolini, L.; Kotar, J.; Di Michele, L.; Cicuta, P. Thermal-driven domain and cargo transport in lipid membranes. *Proceedings of the National Academy of Sciences* **2017**, *114*, 846 LP – 851.
- (12) Parolini, L.; Kotar, J.; Di Michele, L.; Mognetti, B. M. Controlling Self-Assembly Kinetics of DNA-Functionalized Liposomes Using Toehold Exchange Mechanism. *ACS Nano* **2016**, *10*, 2392–2398.
- (13) Parolini, L.; Mognetti, B. M.; Kotar, J.; Eiser, E.; Cicuta, P.; Di Michele, L. Volume and porosity thermal regulation in lipid mesophases by coupling mobile ligands to soft membranes. *Nat. Commun.* **2015**, *6*, 5948.
- (14) Nečas, D.; Klapetek, P. Gwyddion: an open-source software for SPM data analysis. *Cent. Eur. J. Phys.* **2012**, *10*, 181–188.
- (15) Honerkamp-Smith, A. R.; Cicuta, P.; Collins, M. D.; Veatch, S. L.; den Nijs, M.; Schick, M.; Keller, S. L. Line Tensions, Correlation Lengths, and Critical Exponents in Lipid Membranes Near Critical Points. *Biophys. J.* **2008**, *95*, 236–246.
- (16) Veatch, S. L.; Soubias, O.; Keller, S. L.; Gawrisch, K. Critical fluctuations in domain-forming lipid mixtures. *Proc. Natl. Acad. Sci. U. S. A.* **2007**, *104*, 17650 LP – 17655.
- (17) Strauss, M. T.; Schueder, F.; Haas, D.; Nickels, P. C.; Jungmann, R. Quantifying absolute addressability in DNA origami with molecular resolution. *Nat. Commun.* **2018**, *9*, 1600.
- (18) Sample, M.; Matthies, M.; Šulc, P. Hairygami: Analysis of DNA Nanostructure’s Conformational Change Driven by Functionalizable Overhangs. *arXiv* **2023**, <https://doi.org/10.48550/arXiv.2302.09109>, accessed on 2023–03–24.

- (19) Pfeiffer, I.; Höök, F. Bivalent Cholesterol-Based Coupling of Oligonucleotides to Lipid Membrane Assemblies. *Journal of the American Chemical Society* **2004**, *126*, 10224–10225.
- (20) Shen, Q.; Grome, M. W.; Yang, Y.; Lin, C. Engineering Lipid Membranes with Programmable DNA Nanostructures. *Adv. Biosys.* **2020**, *4*, 1900215.
- (21) Rautu, S. A.; Orsi, D.; Di Michele, L.; Rowlands, G.; Cicuta, P.; Turner, M. S. The role of optical projection in the analysis of membrane fluctuations. *Soft Matter* **2017**, *13*, 3480–3483.
- (22) Almeida, P. F. Thermodynamics of lipid interactions in complex bilayers. *Biochimica et Biophysica Acta (BBA)-Biomembranes* **2009**, *1788*, 72–85.
- (23) Hac, A. E.; Seeger, H. M.; Fidorra, M.; Heimburg, T. Diffusion in two-component lipid membranes—a fluorescence correlation spectroscopy and Monte Carlo simulation study. *Biophysical journal* **2005**, *88*, 317–333.
- (24) Sugár, I. P.; Thompson, T. E.; Biltonen, R. L. Monte Carlo simulation of two-component bilayers: DMPC/DSPC mixtures. *Biophysical journal* **1999**, *76*, 2099–2110.
- (25) Lis, M.; Pinal, L.; Swiatek, J.; Cwiklik, L. GPU-based massive parallel Kawasaki kinetics in the dynamic Monte Carlo simulations of lipid nanodomains. *Journal of Chemical Theory and Computation* **2012**, *8*, 4758–4765.
- (26) Schumann, R.; Kobe, S. Criticality condition of the fully anisotropic Ising model with next-nearest neighbour interaction. *Physica A: Statistical Mechanics and its Applications* **2007**, *386*, 187–193.
- (27) Zandvliet, H. J. The 2D Ising square lattice with nearest-and next-nearest-neighbor interactions. *EPL (Europhysics Letters)* **2006**, *73*, 747.

- (28) Onsager, L. Crystal statistics. I. A two-dimensional model with an order-disorder transition. *Physical Review* **1944**, *65*, 117.
- (29) Landau, D.; Binder, K. *A Guide to Monte Carlo Simulations in Statistical Physics*; Cambridge University Press, 2021; pp 51–70.
- (30) Castro, C. E.; Kilchherr, F.; Kim, D.-N.; Shiao, E. L.; Wauer, T.; Wortmann, P.; Bathe, M.; Dietz, H. A primer to scaffolded DNA origami. *Nat. Methods* **2011**, *8*, 221.
- (31) Kim, D.-N.; Kilchherr, F.; Dietz, H.; Bathe, M. Quantitative prediction of 3D solution shape and flexibility of nucleic acid nanostructures. *Nucleic Acids Res.* **2012**, *40*, 2862–2868.
- (32) Schindelin, J. et al. Fiji: an open-source platform for biological-image analysis. *Nat. Methods* **2012**, *9*, 676–682.